ALTERNATING ZONAL JETS IN THE OCEANS: A LABORATORY STUDY

SHEILAGH O'LEARY

Alternating Zonal Jets in the Oceans:
A Laboratory Study

by

Sheilagh O'Leary

A thesis submitted to the
School of Graduate Studies
in partial fulfillment of the
requirements for the degree of
Master of Science

Department of Physics and Physical Oceanography
Memorial University of Newfoundland

January 2011

St. John's Newfoundland

Abstract

This paper investigates anisotropic oceanic features referred to as "zonal jets", zonal meaning that velocity alternates in the east-west direction with latitude. Zonal jets, as predicted by turbulence theory, were recently observed by satellite altimetry in the world ocean and were observed separately in numerical models of the ocean. This study is focused on understanding the mechanisms involved in the formation of alternating zonal jets. Experiments were carried out on a rotating table in the geophysical fluid dynamics laboratory run by Peter Rhines at the University of Washington in Seattle. A cylindrical tank placed on the table and filled with saline water provides a simplified and controlled environment for modeling the dynamics of oceanic circulation. The experiments performed for this study demonstrate a mechanism where the jets result from the development of beta-plumes originating from baroclinic instability at the eastern boundary of an ocean. The underlying dynamics include the propagation of linear and nonlinear basin scale Rossby waves. The dynamic flow fields were measured by Altimetric Imaging Velocimetry (AIV) and optical thickness methods.

Acknowledgements

The past two years have been an extraordinary learning experience for me. Since I was a child I have wanted to learn more about the ocean and after deciding to pursue my Master's degree in physical oceanography I finally had the chance to start satisfying some of my curiosity. I would especially like to thank my supervisor, Yakov Afanasyev, for giving me the opportunity to pursue this degree and for taking me to the University of Washington in Seattle to conduct the experiments that are the basis of this thesis and for his ongoing guidance. I would like to give special thanks to my mom and dad for their support and financial contributions, to Dave Miyata for his "Dedits" and all the hours he put into reading my drafts, Craig Munro for bringing me food and motivation, and to all my family and friends who listened to me talk about my work and acted interested even when they probably weren't entirely sure what I was talking about. I would also like to thank the man from Edmonton for his inspirational talks and encouragement.

Table of Contents

List of Figures

Nomenclature

a – Chromaticity, colour intensity; used to determine the thickness of the injected red fluid layer, h_1 in the Optical Thickness method.

α_{mn} – the n^{th} root of the Bessel function of the m^{th} order

β – beta, used to describe the experimental β parameter; also used in the term β-plane, β-effect and β-plume.

β_E – northward gradient of the Coriolis parameter.

c – Experimental Rossby wave speed; measurement of the speed of the injected fluid.

c_1 – Dimensionless coefficient of the order of unity

c_R – Theoretical calculated Rossby wave speed.

D – Diameter of the circular tank.

f – Coriolis parameter; used in here to describe the effect on a rotating Earth.

f_0 – f_0=2Ω experimental Coriolis parameter for the rotating tank.

γ – Polar β-plane.

g – gravitational acceleration = 9.81 m/s^2.

H – Distance from the surface of the water in the tank to the camera & colour slide

H_0 – Depth of water in the circular tank in the absence of rotation

h_1 – Thickness of the injected red fluid in the experiments.

$h(r)$ – The height of the fluid in the circular tank at radial distance r from the center.

$\vec{k}$ – Vertical unit vector.

k_β – Rhines wavenumber.

κ – Local curvature of the streamlines

L – Characteristic length scale for the experiments, here we selected L=32 cm which is half the tank radius.

L_R – Rhines scale.

λ – The most unstable wavelength.

η – Surface elevation of the fluid as it varies from its initial position at steady state. This is different than the water depth

Ω – Rotation rate of the rotating table.

Ω_0 – Calculated null point rotation rate.

Ω_E – The rotation rate of the Earth

ω – Dispersion relation.

Q – Fluid source.

q – Potential vorticity.

R – Radius of the circular tank.

R_d – Rossby radius of deformation; used here to describe either the barotropic.

R_E – The radius of the Earth.

Ro – Rossby number.

r – Radial distance from the center of the circular tank to any point

S – Burger number.

θ_E – Latitude of the Earth in degrees.

U – Velocity scale.

U_{rms} – Root-mean-square velocity.

V_g – Geostrophic velocity.

V_a – Ageostrophic velocity.

c_1

Chapter 1: Theoretical Background

1.1 Introduction

The circulation of the oceans is a complex system involving many known and some undiscovered processes. Oceanographers who study these systems seek to predict the circulation and identify the mechanisms involved. Satellite altimetry, *in situ* observations of the ocean, numerical modeling, and laboratory experiments are four methods of investigating the oceanic circulation. Alternating zonal (along latitude lines) jets were recently detected by satellite altimetry (Maximenko et al., 2005; Maximenko et al., 2008) and in numerical models (Nakano and Hasumi, 2005; Richards et al., 2006) of the world's oceans. The physical mechanism(s) responsible for the formation of zonal jets has not yet been determined and is a subject of ongoing discussion. The experiments described here were performed at the geophysical fluid dynamics laboratory run by Peter Rhines at the University of Washington in Seattle. The goal of the experiments is to investigate possible mechanisms that may be responsible for the creation of the zonal jets.

In this chapter the theoretical background of jets, turbulence, and barotropic and baroclinic instability is presented, followed by the discovery of the zonal jets, and the different hypotheses about mechanisms that may contribute to the formation of the zonal jets. The second chapter includes a description of the laboratory where the experiments were performed, the experimental apparatus, and the experimental methods used for analysis. The third chapter describes the three experimental set-ups and includes a detailed discussion of the experimental results and conclusions.

1.2 Observations of Zonal Jets in the Ocean

Alternating zonal jets originally predicted by turbulence theory (Rhines, 1975) were recently detected in satellite and in situ observations (Maximenko et al. 2005; Maximenko et al. 2008) and in ocean general circulation models (Galperin et al. 2004; Nakano and Hasumi 2005; Richards et al. 2006). The jets are hidden in the much higher amplitude signal of the variability of the general circulation and can only be revealed by filtering the mean zonal geostrophic velocity field. The zonal jets are shown to populate every part of the world ocean and its marginal seas (Maximenko et al., 2005) and they seem to originate at the eastern boundaries of oceans (Centurioni et al., 2008). The reason for their appearance This section will present the discovery of the zonal jets in the world ocean data and in numerical models. The different theories of what mechanisms are involved in the formation of the jets will be discussed.

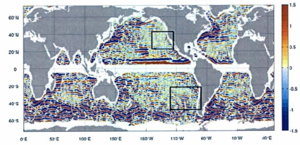

Figure 1: The spatial distribution of the zonal jets in the 1993-2002 mean zonal surface geostrophic velocity field. Units are in cm/s. The zonal jets are the alternating bands of eastward (red) and westward (blue) velocity. The black rectangles outline the two study areas investigated by Maximenko et al, 2008).

The altimetry data used by Maximenko et al. (2005) are 513 weekly maps from October, 1992, to August 7, 2002, of the sea level anomaly. The data was filtered and analyzed to acquire information such as sea level anomaly, which can be used to calculate geostrophic velocity and geostrophic vorticity. The jets are best seen on the map of mean zonal geostrophic velocity (Figure 1) where they appear as jets a few hundred kilometres wide extending over thousands of kilometres (Maximenko et al, 2008). The zonal jets are referred to as 'striations' by Maximenko et al. (2008) because their orientation does not always coincide with the streamlines of the mean flow, meaning that water particles move across rather than along the features. The general interpretation is that the striations are meridionally alternating zonal jets predicted by theory to be generated from two-dimensional geostrophic turbulence on a rotating spherical planet (Rhines, 1975). In this document the 'striations' will be referred to as 'zonal jets'.

Observations show that the zonal jets cross mean geostrophic streamlines and at the crossing point the fluid parcels carried by the flow are deflected slightly in the direction of the jets. This eliminates freely evolving geostrophic turbulence and potential vorticity staircases as possible sources of the jets (Maximenko et al., 2008; Rhines, 1975). Maximenko et al. (2005) averaged geostrophic velocity in one region over 200 weeks (almost four years) and expected that the numerous eddies (also called vortices) passing through the area would cancel each other out, averaging to zero, but the jets remain distinct in the long time average. This indicates that the paths of individual eddies are not completely random and it was hypothesized that the presence of the jets regulates the formation of new eddies which feed back to maintain the jets. This means that eddies following preferred paths or propagating eddies of exceptional strength could be responsible for the zonal jets (Maximenko et al, 2008).

Schlax and Chelton (2008) suggest that zonal jets found in long-term time averages of sea surface height and velocity may be the result of eddies following preferred pathways (eddy artefacts). They mention that zonal jets in previously published studies are most clearly defined where eddy energy variation is the greatest and that the orientations of the jets are consistent with the dominant eddy propagation directions. Another piece of evidence they present is that the anisotropy of velocity variance expected for geostrophic turbulence cannot be detected without long time averages and has been shown to create the illusion of elongated zonal velocity structures. The arguments they present suggest that the zonal jets may be eddy artefacts but it is possible that eddies simply contribute to the persistence of the jets and that the zonal jets are created by another mechanism.

Melnichenko et al. (2010) used 1993-2002 mean dynamic ocean topography, satellite altimeter observations, and results from the Ocean General Circulation Model for the Earth Simulator to study the dynamics of the striations found in the subtropical North and South Pacific. They performed analysis of the relative and potential vorticity budgets of the striations. Their results found that eddy fluxes do not act as a relative vorticity source for the striations but do contribute to the time-mean potential vorticity budget of the jets. This suggests that the jets are not a result of the time averaging of westward propagating eddies but that eddies can propagate along preferred pathways which may coincide with the jets (Scott et al., 2008). Melnichenko et al. (2010) did not isolate a single mechanism being responsible for the formation of the striations and suggest that a complex combination of linear and nonlinear mechanisms might be responsible for their formation.

Centurioni et al. (2008) found evidence in drifter data that the jets are extensions of four stationary meanders of the California Current System (CCS) suggesting that a mechanism analogous to β-plume is responsible for the formation of the zonal jets. The CCS is an eastern boundary current system located in the subtropical North Pacific Ocean that extends from hundreds to thousands of kilometres offshore of the North American coast. The offshore CCS consists of a southward near-surface current that is called the California Current and a deeper poleward undercurrent on the continental rise known as the California Undercurrent.

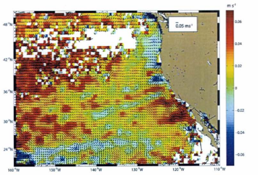

Figure 2: Geostrophic zonal flow with a superimposed vector field (measured by drifters). Four slanted bands of eastward flow (red) originating along the coast can be seen with three alternating weaker bands of westward flow (blue) (Centurioni et al. 2008).

Centurioni et al. (2008) collected velocity observations from Lagrangian drifters drogued at 15 metres depth in the CCS between 1987 and 2005. They used drifter data to compute the mean acceleration and to compare the vorticity flux divergences due to the mean flow and due to eddies. Their observations revealed four permanent meanders in the CCS region that are connected to a set of slanted bands of zonal flow that extend for several thousands of kilometres into the interior of the Pacific Ocean (Centurioni et al., 2008). The unbiased version of the geostrophic velocity field in Figure 2 shows four permanent meanders with typical velocities on the order of 5 cm/s (the red bands). The four convergent flowing jet-like features were tilted northward from the coast. Their results suggested that forcing of the flow due to vorticity fluxes is likely and they recommended further study of the influence of vorticity fluxes on the observed bands of zonal flow.

Chelton et al. (2006) studied the westward energy propagation in the ocean by merging two data sets of sea surface height (SSH) variation that was collected by the TOPEX/POSEIDON (T/P) altimeter from September 1992 to October 2005 and by the European Remote Sensing (ERS-1 & ERS-2) satellites from September 1992 to August 2002. Their study was performed to determine if transient adjustment of the large-scale circulation of the ocean is caused by the westward propagating linear Rossby waves or by nonlinear dynamical processes (Chelton et al., 2006). The combined T/P-ERS data has approximately double the spatial resolution than the previously studied T/P data which permits an investigation of the dispersive character of Rossby waves, which is the dependence of wave frequency on zonal wavenumber. Their analysis detected the expected westward propagation in all ocean basins and found that the propagation speeds outside the tropics (23° both N and S) are faster than the phase speeds predicted by the classical theory for freely propagating linear Rossby waves. Furthermore, they found that the westward propagation tends to be nondispersive and contains many eddy-like structures suggesting that nonlinear dynamical processes may be important. In contrast to linear waves nonlinear eddies can transport momentum, heat, chemical constituents and contribute to the general circulation and large scale water mass distributions (Chelton et al., 2007). It is important to note that Rossby waves can produce nonlinear eddies as a result of wave breaking or by exciting smaller solitary waves and vortices. Observations of eddy propagation show that eddies have a strong tendency to propagate west (Chelton et al., 2006). The generation mechanism for the observed eddies remains an open question. It is widely accepted that nonlinear processes are important in regions of narrow, intense currents, such as areas near western boundary currents or the Antarctic Circumpolar Current (Chelton et al., 2006).

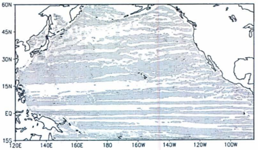

Figure 3: Five-year averaged zonal velocity (cm s^{-1}) at 1000 m for PCF6sine. Contour intervals are 2 cm s^{-1}. Shade indicates westward velocity (Nakano and Hasumi, 2005).

Nakano and Hasumi (2005) investigated the possible origin of zonal jets in an eddy-permitting model of the North Pacific. They used the free-surface version of the Center for Climate System Research (CCR) Ocean Component model (COCO) for calculation. The model solves the primitive equations on a spherical coordinate system. The model incorporates schemes, including isopycnal diffusion, biharmonic horizontal diffusion, a tracer advection scheme, and enstrophy conservation and biharmonic friction in the momentum equations, that enable mesoscale eddies in the eastern portion of the basin to survive while efficiently damping vorticity along the strong western boundary current. They found that zonal jets in their study had common features with the zonally elongated flows obtained in previous modeling studies conducted in isolated basins. In their simulations they found that most of the zonal jets are created by the rectification of turbulent processes on a β-plane, also known as the Rhines effect. The meridional scale of the jets was consistent with the Rhines wavenumber

$$k_\beta = \sqrt{\beta_E / U_{rms}} \tag{1.1}$$

where U_{rms} is the root-mean-square particle speed, and β_E is the north–south gradient of the Coriolis frequency. The inverse of the Rhines wavenumber is the Rhines scale $L_R = \sqrt{U_{rms}/\beta_E}$ which is the characteristic length scale that marks the cross-over between waves and turbulence (Vallis, 2006). At large scales the β-term is dominant and at smaller scales the advective term is dominant (turbulence). The basic pattern for the zonal flows obtained in the different resolution models is largely consistent with observations of the world ocean. The jet-like features can be found in the flow fields of high resolution ocean models averaged over a few years. The zonal jets are coherent over many degrees of longitude and have a relatively small meridional scale of 3-5° (Galperin et al. 2004; Nakano and Hasumi 2005; Richards et al. 2006). Richards et al. (2006) examined the spatial and temporal properties of the zonal jets in a high resolution model of the Pacific Ocean. A vertical meridional section is shown in Figure 4, from Richards et al. (2006), demonstrating that the jets have a large vertical coherency that extends throughout the total depth of the ocean in some regions. The jets extend vertically as compared with the broad zonal flow that slants northward with increasing depth. Some of the zonal jets are explained by the linear response to the local wind stress; other zonal jets are formed without small-scale variation and are presumably created by the Rhines effect. A main conclusion of their work was that the horizontal variation of the meridional scale of the jets is consistent with horizontal variations of the Rhines scale (Richards et al., 2006).

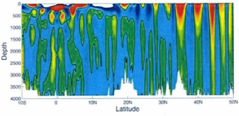

Figure 4: Zonal component of velocity along 180°E averaged over 3 years from the climatological run of the POP model as a function of latitude and depth. Colour saturates at -0.06 m s^{-1} (blue) and 0.08 m s^{-1} (red) (Richards et al., 2006).

Results based on satellite and model data require a thorough validation of oceanic observations before the initial results can be trusted, and modeling these features in a laboratory experiment may help identify the mechanisms that generate zonal jets. The following portion of this chapter will give background information on jets, turbulence, and barotropic and baroclinic instability.

1.3 The Formation of Jets

The physical mechanism responsible for the formation of zonal jets has not yet been determined and is a subject of ongoing discussion. Several different mechanisms have been hypothesized to contribute to the formation of the jets. These mechanisms can be either linear or nonlinear. The linear mechanisms hypothesized to contribute to the formation of zonal jets include stationary Rossby waves (Maximenko et al. 2008), radiating instabilities of eastern boundary currents (Hristova et al. 2008) and linear β-plumes (Centurioni et al. 2008). The nonlinear mechanisms include the jets being eddy artefacts (Schlax & Chelton 2008), the result of eddies following preferred pathways (Scott et al. 2008), eddy forcing terms (Melnichenko et al. 2010) and the Rhines mechanism (Rhines 1975).

The hypotheses that suggest purely linear dynamics are responsible for the formation of the jets have not been confirmed to be solely responsible for the creation of the zonal jets. Melnichenko et al. (2010) suggest that nonlinear effects are essential in the dynamics of the jets by showing that the eddy forcing (advective) terms are as important as the linear terms in both relative and potential vorticity balances. Before satellite altimetry, the detection of these zonal jets was difficult because only satellites provide long-term, large-scale coverage at fine enough horizontal resolution to reveal the jets. The zonal jets were found to populate every part of the world ocean, including isolated basins. An interesting property of zonal jets is their orientation does not always coincide with the streamlines of the mean flow so water particles move across rather than along them.

Jets are an extreme form of the mean circulation: localized, elongated, energetic flows, usually with persistence in time (Rhines, 1994). In classical fluid dynamics, jets owe their existence to boundary conditions, such as an injection of both mass and momentum from a nozzle. In natural fluid flows of large scale, jets occur in the nearly horizontal circulations of the oceans and atmospheres of the large planets. The two mechanisms that can lead to the formation of zonal jets that are of interest here are β-plumes and two-dimensional turbulence. The theory of β-plume dynamics discussed by Stommel (1982), Davey and Killworth (1989), Pedlosky (1992), Rhines (1994), Spall (2001), and Spall & Pickart (2003) will be presented. We will emphasize two mechanisms: β-plume dynamics and the formation of jets from eastern coastal currents by baroclinic instability, which is discussed in section 1.5.

1.3.1 Rhines/Turbulence Theory

The tendency of two-dimensional turbulence to form zonal jets was first presented by Rhines (1975). In the pioneering paper by Rhines (1975) it was shown that a homogeneous cascade of two-dimensional turbulence tends towards a flow of alternating zonal jets which are almost perfectly steady. In the context of small-scale turbulence, the underlying mechanism of jet formation is the rectification of zonal jets by the emission of Rossby waves. For this mechanism the important length scale is the Rhines scale $L_R = \sqrt{U_{rms}/\beta}$ which marks the boundary between turbulence and Rossby waves (Rhines, 1975). The conversion of turbulence into waves yields more narrowly peaked wave number spectra and less fine-structure in the spatial maps, while smoothly distributing the energy about physical space.

Planetary rotation and topographical constraints are two factors that lead to quasi-two-dimensionalization of the oceanic circulation on large scales. In the ocean, the large scales are affected by the latitudinal variation of the Coriolis parameter, the planetary vorticity gradient or so-called β-effect. The β-effect breaks the horizontal isotropy of the flow field and facilitates its self-organization in the zonal (east-west) direction giving rise to the emergence of quasi-one-dimensional structures, also known as zonal jets. The basic physics of quasi-two-dimensional turbulence with a β-effect is described by the two-dimensional vorticity equation specified on a β-plane, which is defined below in section 1.3.2. Although this formulation is an idealization of the real-world situations, it allows attention to be concentrated on various features of anisotropic turbulence and its interaction with Rossby waves.

1.3.2 The β-plume Mechanism

The β-plume mechanism is a key concept in the experiments described here. Zonal jets will be formed by creating a forced flow that leads to plume development which then leads to jet formation. In the experiments conducted here the flow is on a β-plane. The explanation for the experimental dynamics is found in Chapter 2 and why the experimental flow is on a polar β-plane. Here I will describe the β-plane approximation and the β-effect on the rotating Earth. On the rotating Earth the magnitude of the vertical component of rotation varies with latitude. This effect can be approximated on the tangent plane by allowing the Coriolis parameter to vary as,

$$f = f_E + \beta_E y$$

Here f is the Coriolis parameter on the rotating Earth, $f_E = 2\Omega_E \sin\theta_E$ where Ω_E is the rotation rate of the Earth and θ_E is latitude in degrees, $\beta_E = \partial f/\partial y = (2\Omega_E \cos\theta_E)/R_E$ where R_E is the radius of the Earth. The β-plane model captures the effect of the Earth's sphericity by a linear variation of the Coriolis parameter in a planar geometry (Vallis, 2006). The β-effect is the dynamical equivalence between the variation of the Coriolis parameter with latitude and variations of topography in the presence of a constant Coriolis force (Pedlosky, 1987). The β-plane can be simulated in a laboratory setting by using a circular tank with a flat bottom with a free fluid surface such that the depth of the fluid varies parabolically with radius.

The tendency of coastal disturbances, including intense jets, eddies, and Rossby waves, created by temperature or salinity gradients to propagate westward along lines of latitude due to the β-effect are called β-plumes (Stommel, 1982; Rhines, 1994). A β-plume is a quasi-zonal gyre-like response to a localized perturbation and is established by the emission of Rossby waves. The β-plume concept was introduced by Stommel (1982) after he studied the β-governed circulation at mid-depth produced by the hydrothermal vents of the South Pacific Rise. He described a thin thermal convective layer governed by the β-plane and driven by heating at the summit of the ridge and suggested that the plume is dynamically active and spreads westward of its own accord and would extend indefinitely westward in the absence of vertical diffusion.

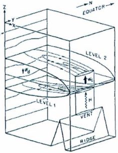

Figure 5: Two oppositely rotating β-plumes can be seen extending westward from the crest of the ridge (Stommel, 1982).

Davey and Killworth (1989) investigated the response of an ocean model to localized buoyancy forcing on a β-plane and found three flow regimes. When the forcing was weak, the response was linear and takes the form of a steady jet-like circulation extending westward from the source with a front propagating at a long Rossby waves speed. When the amplitude is increased, the response changes to a chain of discrete eddies that form in the forcing region and propagate westward. This type of flow was observed in the series of experiments discussed in section 3.2.

Pedlosky (1992) created a model with geostrophic, hydrostatic, and incompressible flow to study the baroclinic structure of the abyssal circulation and the most robust feature of the flow is the tendency for western propagation of baroclinic anomalies by the Rossby wave mechanism. Spall and Pickart (2003) divided the β-plume circulation into three dynamical regimes. The first is the forcing region, in which the balance is between vorticity input from the wind or upwelling and advection across the mean vorticity gradient. For upwelling, the flow in the forcing region is toward the pole. The second dynamical regime is when the flow must be zonal and exists outside of the latitude range of the forcing and away from the meridional boundaries. Neglecting eastern boundary layers, the result is a westward flow just poleward of the forcing region and a returning eastward flow equatorward of the forcing region. These zonal flows are along contours of constant potential vorticity because both the forcing and the dissipation are assumed weak. The third dynamical regime exists where the circulation is assumed to close somewhere to the west in a viscous boundary layer.

The theory presented here follows the theory from the paper by Afanasyev et al. (2010) that was recently submitted to the Geophysical & Astrophysical Fluid Dynamics for publication. Consider a flow induced by a localized perturbation on the polar β-plane where the Coriolis parameter varies quadratically with the distance from the pole,

$$f = f_0(1 + \gamma r^2) \qquad (1.2)$$

Where f_0 is the Coriolis parameter, γ is the parameter for the polar β-plane, and r is the distance from the pole (the center of the tank). The total velocity of the flow can be written as a sum of the geostrophic (subscript g) and ageostrophic (subscript a) components,

$$\vec{V} = \vec{V_g} + \vec{V_a} \qquad (1.3)$$

with geostrophic velocity

$$\vec{V_g} = \frac{g}{f_0}\vec{k} \times \nabla\eta \qquad (1.4)$$

and ageostrophic velocity

$$\vec{V_a} = \frac{g}{f_0^2}\nabla\eta - \vec{V_g}\gamma r^2 \qquad (1.5)$$

Here g is gravitational acceleration, η is the surface elevation and $\vec{k}$ is the vertical unit vector. The shallow water continuity equation, as in Gill (1982), can be used to introduce a source Q to the right-hand side of the equation

$$H_0\left(\frac{\partial u_a}{\partial x} + \frac{\partial v_a}{\partial y}\right) + \frac{D_g}{Dt}\eta = Q \qquad (1.6)$$

where H_0 is the water depth, subscript a denotes ageostropic terms and subscript g denotes geostrophic terms. Substituting (1.4) into (1.5) then linearizing the advective derivative and transferring into polar coordinates (r, θ)

$$\nabla^2\eta_t - \frac{f_0^2}{gH_0}\eta_t + 2\gamma f_0\eta_\theta = -Q\frac{f_0^2}{gH_0} \tag{1.7}$$

Now look for the solution of equation (1.6) of the form

$$\eta = \sum_{m=-\infty}^{+\infty}\sum_{n=1}^{\infty}\eta^{mn}exp(im\theta)J_m\left(\alpha_{mn}\frac{r}{R}\right) \tag{1.8}$$

where α_{mn} is the n^{th} root of the Bessel function of the m^{th} order and R is the radius of the domain (the radius of the tank). Substituting into equation (1.6) we obtain

$$\eta_t^{mn}\left(-\alpha_{mn}^2 - \frac{f_0^2}{gH_0}\right) + 2\gamma f_0 im\eta^{mn} = \frac{f_0^2}{gH_0}Q_{mn} \tag{1.9}$$

where Q_{mn} is the Fourier-Bessel transform for the source

$$Q = \sum_{m=-\infty}^{+\infty}\sum_{n=1}^{\infty}Q_{mn}exp\,(im\theta)J_m\left(\alpha_{mn}\frac{r}{R}\right) \tag{1.10}$$

such that (Arfken and Weber, 2001)

$$Q_{mn} = \frac{1}{2\pi}\frac{2}{R^2[J_{m+1}(\alpha_{mn})]^2}\int_0^{2\pi}d\theta\int_0^R Q(r,\theta)exp(-im\theta)J_m\left(\alpha_{mn}\frac{r}{R}\right)rdr$$

Integrating equation (1.7) with initial condition η^{mn}=0 at t = 0, we obtain

$$\eta^{mn} = \frac{-4iQ_{mn}}{mf_0}\left(1 - e^{i\omega_{mn}t}\right)$$

with dispersion relation

$$\omega = \frac{2m\gamma f_0}{\frac{\alpha_{mn}^2}{R^2} + \frac{f_0^2}{gH_0}} \tag{1.11}$$

The solution of equation (1.6) is then

$$\eta = -i\frac{4}{f_0}\sum_{m=-\infty}^{+\infty}\sum_{n=1}^{\infty} Q_{mn}\left(1 - exp(i\omega_{mn}t)\right)exp(im\theta)J_m\left(\alpha_{mn}\frac{r}{R}\right) \tag{1.12}$$

This solution is similar to that obtained by Davey and Killworth (1989) for the β-plane. A long wave solution can be easily obtained if the term responsible for dispersion ($\nabla^2\eta_t$) is ignored in equation (1.6). The solution is given in the form of the integral

$$\eta = \frac{4}{f_0}\int_{\theta}^{\theta+2\gamma f_0 R_d^2 t} Q(r,\theta')d\theta' \tag{1.13}$$

Alternatively the solution is given by (1.11) with a simplified dispersion relation yielding non-dispersive waves that propagate purely azimuthally (to the west)

$$\omega_{mn} = 2m\gamma f_0 R_d^2$$

However, if the full dispersion relation (1.10) is used, the solution given by (1.11) is quite different. The wave is much slower and dispersion is very significant. The ratio of the terms in the denominator in (1.10) is

$$\frac{\alpha_{mn}^2 gH_0}{R^2 f_0^2} = \alpha_{mn}^2\frac{R_d^2}{R^2}$$

where $R_d = (gH_0)^2/f_0$ is the barotropic Rossby radius of deformation. In our experiments R_d = 18 cm and the radius of the tank is 65 cm. With α_{mn} starting at 2.4 and increasing with indices m and n the dispersion term becomes dominant. If the dynamics of the plume is determined by the baroclinic Rossby waves the radius of deformation can be much smaller and the plumes can be more concentrated as a result. In the experiments described here barotropic Rossby waves and baroclinic dynamics, which are controlled by the lower layer in a two-layer fluid, were observed.

1.3.3 Barotropic & Baroclinic Instability

Here I will describe two types of instability that will play a role in the experiments. The phenomenon of instability is the preferential transfer of energy from the wave-free flow to the fluctuating flow (Pedlosky, 1987). The two types of instability that will be observed in the experiments are barotropic and baroclinic instability. Barotropic instability depends on the existence of the horizontal shear of the basic current and can occur in a homogeneous fluid in the absence of vertical shear (Vallis, 2006). Barotropic instability involves the northward gradient of the Coriolis parameter and it dominates in the tropics because midlatitude disturbances are more influenced by the baroclinic instability. Baroclinic instability arises in rotating, stratified fluids that depends on the existence of the vertical shear of the basic current (Vallis, 2006). In baroclinic instability small perturbations of the basic steady flow generate large-scale waves. The baroclinic instabilities appear to propagate as Rossby waves but their erratic and unexpected appearance suggests that they are not generated by any external forces but are due to an inherent instability of midlatitude eastward flows. The energy source for the instability is the available potential energy of the basic flow (Pedlosky, 1987). The presence of a horizontal temperature or salinity gradient implies that baroclinic instability occurs in a two-layer fluid and varies with depth. The horizontal gradient is unstable because it can release the stored potential energy by means of an instability that would cause the density surfaces to flatten out. In the process, vertical shear of the mean flow would decrease and perturbations would gain kinetic energy. The β-effect is not an essential requirement of the instability but it does modify the behaviour of the instability.

The Rossby radius of deformation is the horizontal scale at which rotation effects become as important as buoyancy effects (Gill, 1982). Baroclinic instability is of central importance to eddy production in midlatitude oceans and atmospheres at the scale of the baroclinic Rossby radius of deformation. In the experiments performed here, the equation for the Rossby radius of deformation is

$$R_d = \sqrt{\frac{g\Delta\rho H_0}{\rho}}\frac{1}{f_0} \qquad (1.14)$$

where g is the acceleration due to gravity, $\Delta\rho$ is the density difference between the source fluid and tank fluid, H_0 is the initial height of fluid in the tank in the absence of rotation, ρ is the density of the tank fluid, and $f_0 = 2\Omega_0$ is the Coriolis parameter, and Ω_0 is the null point rotation rate of the tank. Linear theory gives that the most unstable wavelength λ is proportional to the Rossby radius of deformation,

$$\lambda = c_1 R_d \qquad (1.15)$$

where c_1 is the dimensionless coefficient of the order of unity. For the single-layer experiments described here c_1 has a value ranging from 2 to 5 with an average barotropic R_d of 18 cm and an average baroclinic R_d of 2.6 cm.

1.4 Concluding Remarks

This study supports the theories of Centurioni et al. (2008) that the zonal jets are extensions of meanders by a β-plume mechanism. Support will also be given to the theories of Nakano and Hasumi (2005) regarding the Rhines effect and how it contributes to the formation of zonal jets and to the theory of Melnichenko et al. (2010) that different mechanisms operate simultaneously to create the jets.

Chapter 2: Experimental and Analytical Method.

2.1 Introduction

The experiments were performed at the geophysical fluid dynamics (GFD) laboratory operated by Peter Rhines at the University of Washington in Seattle. This laboratory contains a rotating table that is installed on a vibration reducing floor that is isolated from the rest of the building to minimize the effect of vibrations on the experiments. The rotation rate of the platform is controlled by a computer. A circular tank is placed on the rotating table and is filled with fluid (either fresh or salt water depending on the experiment, see Appendix A). The experimental flows are induced by sources of buoyancy. The dynamic fields created by the experimental flow are measured by a laboratory technique similar to satellite altimetry. In this chapter the laboratory apparatus and experimental techniques will be described.

2.2 Laboratory Apparatus & Experimental Techniques

The tank was rotated in the anticlockwise direction with a vertical axis through its center at rate Ω=1.89 rad/s. One rotation of the tank is equal to one laboratory "day". This means each tank rotation models one day of circulation in the ocean. The number of rotations or lab "days" is calculated by using the relation that 1.89 rad/s is equal to 0.3 tank rotations per second. A colour slide is located at height H above the surface of the water and is slightly off the rotation axis, which is also the optical axis of the paraboloid. A fluorescent lamp illuminates the colour slide from behind and creates a uniform reflection on the parabolic fluid surface. The reflection of the slide in the water is observed by a video camera that is located at height H above the water and is centered above the rotation axis. One of two different cameras was used to record the experiments: the first was a Sony DCR-HC96 video camera and the second was an Aptina camera. The Sony camera provided continuous video with the frame rate of 30-fps with relatively low spatial resolution of 480x760 pixels. The Aptina camera has a Micron 3 megapixel sensor and captured still images with high spatial resolution and was able to output the uncompressed RGB color signals. A sketch of the experimental set-up is shown in Figure 6.

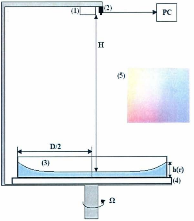

Figure 6: The experimental setup: Fluorescent lamp box with colour slide (1), camera (2) connected to a PC, rotating tank (3), lamp box for optical thickness measurements (4), insert showing the RGB colour slide (5). H is the distance from the colour slide and camera to the surface of the rotating fluid, D is the diameter of the tank, Ω is the rotation rate of the platform, h(r) is the height of the fluid at radial distance r from the centre of the tank (shown here when r=D/2). Note the parabolic shape of the fluid surface.

The reflection law can be used to calculate the null point rotation rate $\Omega_0 = \sqrt{g/H}$. In this experiment the calculated null point is 1.94 rad/s using H=2.6 m and g=9.81 m/s^2. This value is close to the rotation rate of 1.89 rad/s that was used during the experiments. The analysis of the experiments involved the use of altimetric imaging velocimetry (AIV) and optical thickness methods. For details on the AIV method see Afanasyev et al. (2007). The AIV and optical thickness software is used in Matlab (The Mathworks Inc.) and was developed by Y. Afanasyev. The software is used to calculate the variables of interest from still images extracted from videos of the experiments. The still images of the flows are used to take measurements of different flow features, such as wavelength. In this chapter, the laboratory set-up and measuring techniques employed in the experiments are described.

The polar β-plane was simulated by rotating a cylindrical container of water with a free surface such that the depth of the layer varies parabolically with radius. The free surface of the rotating fluid is a paraboloid described by

$$h(r) = H_0 + \frac{\Omega^2}{2g}\left(r^2 - \frac{D^2}{8}\right) \qquad (2.1)$$

where $h(r)$ is the height of the free surface, H_0 is the depth of the water layer in the absence of rotation, Ω=1.89 rad/s is the rotation rate, g is gravitational acceleration, r is the radial distance from the axis of rotation on the horizontal plane, and D is the diameter of the tank.

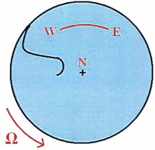

Figure 7: Sketch showing the directions in the tank. The circular tank rotates in an anticlockwise direction and models the northern hemisphere. The center of the tank is the polar region (North) and the wall of the tank is the equator (South). The East (clockwise) and West (anticlockwise) directions are indicated. The black line in the tank represents the barrier that was used in some of our experiments. Flows propagating away from the Eastern side are moving towards the West.

As mentioned in the first chapter one of the most valuable new tools of observational oceanography is satellite altimetry that is used to measure the sea-surface height and thus the subsurface hydrostatic pressure by timing a radar beam pulsed from above. In the rotating tank filled with homogeneous-density fluid dominated by geostrophic, hydrostatic, barotropic motions, the interior circulation is two-dimensional and is fully described by the slope of the free surface elevation, η. In a laboratory setting η is a field of great interest because the variations of pressure due to the flow cause perturbations of the slope. Geostrophic balance relates the gradient of pressure to the velocity field and therefore provides the valuable characteristics of the flow. For a rotating fluid, the dynamical relations can be used to obtain all the major fields including the velocity, relative vorticity, potential vorticity, and surface elevation. The methods of obtaining these fields will be presented in the following section.

2.3 Altimetric Imaging Velocimetry

The experimental analysis was performed using AIV and optical thickness software. The software calculates the main fields of geostrophic velocity and surface elevation, η, for the entire fluid surface. All other variables can be calculated using these two fields, including quasigeostrophic velocity, geostrophic and quasigeostrophic vorticity. The AIV method employs optical altimetry techniques (Rhines et al., 2006) combined with a colour coding method. The optical altimetry method uses a white light source that is reflected from a position above the free surface. The geometry of the free surface paraboloid in solid-body rotation can be used to provide the amplified image of the surface and measure the slope components of surface elevation. Imperfections in the surface of the telescope, created by fluid motion and disturbances, appear as disturbances on the reflected surface. Quantitative maps, images, and animations of surface elevation relative to the mean paraboloid can be obtained. AIV combines color coding with optical altimetry and allows the measurement of two components of the gradient of surface height.

The AIV colour coding of the surface is achieved by placing a colour slide that has a two-dimensional colour gradient (in the x and y direction) in front of an LED light panel. An image of the colour slide is shown in Figure 6. When the fluid has reached steady state at the experimental rotation rate Ω the slide is infinitely stretched over the surface of fluid (Figure 8) such that one observes the entire surface of fluid to be the same colour which corresponds to the center of the slide.

The observed variation of colour results from the reflection of the perturbed surface of fluid. Each colour corresponds to a vector composed of x- and y-components of slope and thus effectively provides the gradient of surface pressure. Any local perturbation of the surface will change its slope and a different colour will be reflected.

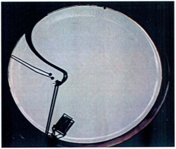

Figure 8: In this image the tank is rotating at the speed Ω=1.89 rad/s. No flow is induced. Only one colour from the colour slide is being reflected over the entire surface of the rotating fluid. The dark curved line is a barrier placed in the tank.

The polar β-plane or γ-plane is simulated in a laboratory setting by rotating a cylindrical container of water with a free surface such that the depth of the layer varies parabolically with radius. In these experiments the bottom of the tank is flat. On large scales, the circulation of the ocean is affected by the latitudinal variation of the Coriolis parameter, the 'planetary' vorticity gradient, the linear approximation of which in midlatitudes is also called the β-effect. This effect can be captured in the β-plane approximation in which a portion of the spherical surface is replaced by a tangential plane (Pedlosky, 1987).

The surface slope $\left(\frac{\partial \eta}{\partial x}, \frac{\partial \eta}{\partial y}\right)$ is the primary dynamic field measured by AIV. The reflected colour will correspond to its particular location (X, Y) on the slide. Here the coordinates X and Y are measured from the center of the slide. The vector of the slope of the surface can then be obtained,

$$\left(\frac{\partial \eta}{\partial x}, \frac{\partial \eta}{\partial y}\right) = \frac{1}{2r}(X, Y) \tag{2.2}$$

where η is the free surface height, r is the radial distance from the axis of rotation (tank center) on the horizontal plane. The velocity field can then be calculated using the geostrophic relation,

$$f_0 \vec{k} \times \vec{V}_g = -g\nabla\eta \tag{2.3}$$

which is an approximation of the equation of motion and provides the balance between the Coriolis force and the gradient of pressure. Here $\vec{k}$ is the vertical unit vector and $f_0 = 2\Omega_0$ is the Coriolis parameter. The geostrophic balance provides a leading approximation to the equation of motion in the system where the relative vorticity is small compared to the background vorticity (ie: small Rossby number). The geostrophic velocity is then calculated as follows

$$\vec{V}_g = \frac{g}{2\Omega_0}\left(-\frac{\partial \eta}{\partial y}, \frac{\partial \eta}{\partial x}\right) \tag{2.4}$$

The gradient wind relation is given by

$$\vec{k} \times \vec{V}(\kappa V + f_0) = -g\nabla\eta \tag{2.5}$$

where κ is the local curvature of the streamlines and can be used to calculate the velocity field. The curvature of the tangent line to the velocity vector $\vec{V}$ is a scalar field given by the magnitude of the vertical component of the curl of the normalized velocity vector, $\kappa = \mathrm{curl}_z(\vec{V}/V)$. This is different from the vorticity, defined as $\zeta = \mathrm{curl}(\vec{V})$ because the definition of curvature only includes the information about the direction of the velocity vector rather than its magnitude. The gradient wind relation includes a centripetal acceleration term which is quadratic in velocity. This term approximates nonlinearity for the flows being close to a steady state. The relative magnitude of this term is of the order of the Rossby number, $\mathrm{Ro} = |\zeta|/f_0$. The curvature field can be estimated from the geostrophic velocity field in the first approximation. The gradient wind velocity is determined using the last equation

$$\vec{V} = \vec{V}_g - \kappa \frac{V_g \vec{V}_g}{f_0} \tag{2.6}$$

The next level of approximation includes relatively small nonlinear and unsteady terms as follows

$$\vec{V} = \frac{g}{f_0} \vec{k} \times \nabla\eta - \frac{g}{f_0^2} \nabla\eta_t - \frac{g^2}{f_0^3} J(\eta, \nabla\eta) \tag{2.7}$$

where J is the Jacobian. Equation (2.7) is used in the AIV method to calculate the velocity field from the measured slope vector. Two consecutive images of the flow are required to calculate the time derivative but one image of the flow is enough to calculate the geostrophic velocity.

Although even strongly baroclinic flows always have a pressure signature on the surface which can be measured by AIV additional information about the flow is often required. The topography of the surfaces of constant density and the thickness of the fluid layers between them are essential components of the flow dynamics. The AIV method is used to determine the surface velocity of the fluid and when it is combined with optical thickness method the velocity fields in both layers of fluid can be measured and a more complete understanding of the experimental flow can be obtained.

2.4 Optical Thickness Method

The optical thickness method is used when there are two layers of fluid in the flow. In the experiments performed here the tank contains a single layer of fluid and a source injects fluid that is coloured with dye that forms a second fluid layer. When the optical thickness method is combined with the AIV method the high resolution velocity fields in two layers, surface elevation, and the depth of the interface can be obtained. The optical thickness method requires the use of a dye so the thickness of the layer can be measured. The thickness of the dyed layer, h_1, can be measured by relating the value of the chromaticity, a, to the thickness of the dyed fluid. To obtain a value for chromaticity a small cuvette with a sloping bottom was placed above the surface of the water for the purpose of calibration. The cuvette contained the same red-dyed water that was injected into the tank by the source. The profile of the chromaticity, a, across the cuvette gives a relation between the depth of the fluid in the cuvette and its colour intensity. This relation is used to calculate h_1 in every pixel of the experimental image.

Almost simultaneous measurements of AIV and optical thickness methods are achieved by switching illumination of the tank from the colour slide above the tank to the uniform lights below the tank. The transition time is ~3 seconds between surface reflection and tank illumination. In all the experiments, the water injected from the source was dyed a red colour by food dye and the water in the tank was transparent. The ratio of dye to water in the source fluid was 2 mL of red dye for 3 L of water.

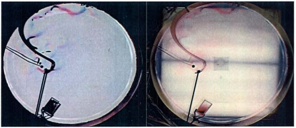

Figure 9: The left image shows the surface of the tank reflecting the colour slide. On the right, the tank is illuminated from below and the dyed fluid can been seen.

The quadratic variation (γ-effect) of the Coriolis parameter provides a good approximation for the polar regions of the rotating planets while linear variation (β-effect) describes the midlatitudes. The variation of the Coriolis parameter is difficult to model directly but this effect can be emulated by varying the depth of the fluid layer. The dynamical equivalence between the variation of the Coriolis parameter and the variation of the total depth of the fluid later is a consequence of the conservation of the potential vorticity (PV). In a one-layer fluid the approximate expression for PV can be written as follows:

$$q = \frac{1}{H_0}\left[\zeta + 2\Omega_0\left(1 - \frac{\Omega_0^2}{2gH_0}\left(r^2 - \frac{D^2}{8}\right)\right)\right] \tag{2.8}$$

where the equation defining $h(r)$ was used for the total depth of the layer. The parameter γ can be defined as the coefficients in front of the term proportional to r^2 in the above PV equation:

$$\gamma = \frac{\Omega_0^3}{gH_0} \tag{2.9}$$

The experimental value of β with units in (cm^{-1} s^{-1}) was calculated using

$$\beta = f_o \frac{\frac{\Omega^2}{g} L}{H + \frac{1}{2}\frac{\Omega^2}{g}\left(r^2 - \frac{1}{2}R^2\right)} \tag{2.10}$$

where Ω (s^{-1}) is the rotation rate of the tank, g (cm s^{-2}) is the gravitational constant, L (cm) is approximately half of the tank radius (taken here to be 32 cm), H (cm) is the thickness of the fluid layer without rotation, and R (cm) is the radius of the tank.

In a two-layer flow, the dynamics are more complicated (relative to a one-layer flow) and the γ-effect is due to the variation of the total depth of the fluid for barotropic motions only. The depth of the fluid layer in our case is determined by the parabolic form of the surface. For the upper layer of a two-layer fluid (in these experiments, the injected red freshwater fluid will rise to the surface of the higher-density saltwater in the tank), it is clear that for purely baroclinic motions when fluid columns in the upper layer are displaced, the height of the columns is not affected by the form of the surface. This is because the columns move along the parabolic equipotential surfaces that are parallel to the free surface. Thus, the uniform potential vorticity upper-layer flow is not influenced by γ-effect unless the columns in the lower layer mimic the motion of the upper layer. A barotropic component of the flow which is by definition the same in both layers provides a mechanism by which the flow in both layers will be subject to (topographic) γ-effect. The importance of the barotropic component is emphasized by writing the equations for the hydrostatic two-layer system in the form (Afanasyev et al., 2009):

$$\vec{u}_{1t} + \vec{u}_1 \cdot \nabla\vec{u}_1 + f_0\vec{k} \times \vec{u}_1 = -g\nabla\eta \quad (2.11)$$

$$h_{1t} + \nabla \cdot (\vec{u}_1 h_1) = 0 \quad (2.12)$$

$$\vec{u}_{2t} + \vec{u}_2 \cdot \nabla\vec{u}_2 + f_0\vec{k} \times \vec{u}_2 = -\nabla(g\eta - g'h_1) \quad (2.13)$$

$$-h_{1t} + \nabla \cdot [\vec{u}_2(h - h_1)] = 0 \quad (2.14)$$

where $\mathbf{u}_i$ is the layer *i* velocity, h_1 is the upper layer thickness, h is the total fluid thickness given by (2.1) and g' is the reduced gravity. Geostrophic velocity in a two-layer system can be easily obtained from equations (2.11) and (2.13),

$$f_0\vec{k} \times \vec{u}_1 = -g\nabla\eta \quad (2.15)$$

$$f_0\vec{k} \times \vec{u}_2 = -\nabla(g\eta - g'h_1) \quad (2.16)$$

Equations (2.15) and (2.16) are the analogue of the geostrophic relation given by equation (2.3) and are used here to calculate the geostrophic velocity in both layers from the measured fields of $\nabla\eta$ and h_1.

Chapter 3: Experimental Results & Discussion.

3.1 Introduction

This study is focused on understanding several mechanisms involved in oceanic circulation and their role in the formation of alternating zonal jets. The mechanisms include the β-plume mechanism, Rossby waves, barotropic and baroclinic dynamics, and nonlinear dynamics. The mechanisms of interest were recreated in a series of experiments that were performed in January 2009 in the fluid dynamics lab at the University of Washington in Seattle. Three different experimental setups were employed. This chapter is partially based on the paper by Afanasyev et al. (2010).

The first experimental set-up models a simple β-plume (Stommel, 1982; Davey & Killworth, 1989; Rhines, 1994) by injecting water from a point source into the surface of saline fluid in the tank. A pump moves the source fluid through a tube and the fluid was injected into the tank through a circular sponge diffuser that was attached to the end of the tube. In the second experimental set-up, an eastern barrier is created by placing a wall that ran from the 'equator' (ie: the tank wall) to the 'polar regions' near the center of the tank. The fluid source was located where the barrier meets the tank wall and fresh water is injected onto the surface of the saline fluid in the tank through a wedge-shaped sponge diffuser. The red source fluid creates an eastern boundary jet and through processes involving the β-plume mechanism and baroclinic instability, the flow eventually creates zonal jets. It will be demonstrated that the laboratory model correctly reproduces the main features of the circulation in the North Pacific that are responsible for the formation of the zonal jets.

In the third experimental set-up, a linear source is placed in the radial direction along the midlatitude region of the tank at the bottom of the tank. This experiment is designed to demonstrate the main features of a plume and avoid the preset length scale of plumes that is controlled by the size of the coastal meanders, as in the barrier experiment.

The resulting flows of the three experimental set-ups will be described in sections 3.2, 3.3, and 3.4. Section 3.5 will present the analysis that was performed to investigate the flows created by the three experimental set-ups. This includes a discussion of the control parameters of the flow and the measurement techniques that were used. Section 3.6 will conclude the chapter with a detailed discussion of the results.

3.2 Point Source β-plume Model

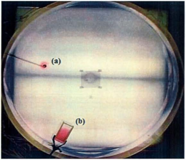

Figure 10: Point source experimental set-up. The source is a sponge attached to a glass tube (a) and the cuvette (b) is filled with red-dyed fluid and is used for calibration in the Optical Thickness method. It was used in all the experiments.

This experiment models a simple β-plume (Stommel, 1982; Davey & Killworth, 1989; Rhines, 1994) by injecting water from a point source into the surface of saline fluid in the tank. In this experiment the source was a circular sponge diffuser that was placed in the midlatitude regions of the tank a few centimetres above the tank bottom. The volume flow rate was in these experiments was 0.015 L/s (see Table 3 in Appendix A). After the pump is turned on the injected source fluid creates a chain of anticyclonic eddies (Figure 11 b, c) that connect to form a β-plume that flows westward along the midlatitude regions of the tank (Figure 11 d). The effects of a chain of anticyclonic eddies is to retard their westward propagation because of the interactions between eddies as they propagate (Davey and Killworth, 1989). The flow regime observed in these experiments is the second flow regime discussed by Davey & Killworth (1989) when a chain of discrete eddies forms the westward propagating flow rather than a uniform tube of fluid propagating to the west, as would be observed if the forcing was weaker. Baroclinic instability governs the dynamics and forms the meanders and eddies that propagate westward (Figure 11 c).

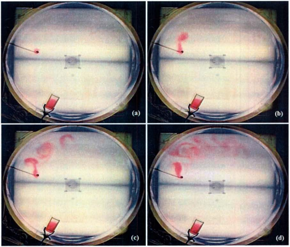

Figure 11: Images from experiment #2 on January 15, 2009 showing the development of the β-plume. (a) 0 days [t=0 s], (b) 6 days [t=20 s], (c) 18 days [t=60 s], and (d) 36 days [t=120 s].

3.3 Eastern Boundary Experiments

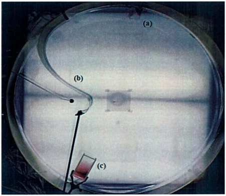

Figure 12: Eastern boundary experimental set-up. The source is a small plexiglass triangle containing a sponge attached to a glass tube (a), the eastern boundary is a curved piece of aluminum (b), and the cuvette (c). The source fluid will enter the tank from the left side of the source and propagate towards the eastern boundary.

This series of experiments was designed to demonstrate the development of β-plumes formed by the quasi-permanent meanders at the eastern boundary. In satellite altimetry images the eastern boundary source for mesoscale eddies is strongly evident and often begins with a north-south ridge of pressure propagating offshore before collapsing into nonlinear Rossby waves/eddies. At some sites it appears to be a direct instability of the eastern boundary current. This hypothesis was recently discussed by Centurioni et al. (2008) regarding meanders of the California current. In this experimental set-up the eastern boundary is an aluminum barrier that was placed in an approximately radial direction (North-South). The wedge-shaped diffuser was placed at the fluid surface at the tank wall (the equator) and injects source fluid into the tank. In each trial for this experiment, the source fluid was freshwater and the salinity of the tank was varied from 15‰ to 30‰ to observe the effects of salinity on the dynamics of the resulting flow.

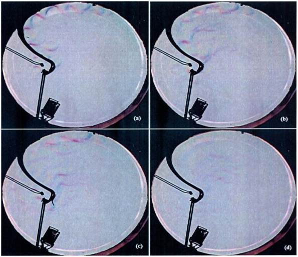

Figure 13: Development of zonal jets in experiment #2 from January 16, 2009. (a) 36 days [t=120 s], (b) 115 days [t=385 s], (c) 202 days [t=674 s], and (d) 303 days [t=1012 s].

The source fluid developed into a narrow boundary current that propagated cyclonically and followed the eastern barrier and had similar dynamics to the California Current in the North Pacific. The current becomes unstable and forms baroclinically unstable meanders (Figure 13 a) along the tank wall and the eastern boundary. As the tank continues to rotate and the source continues to contribute fluid to the stationary meanders, the resulting circulation is extended westward by the β-effect and is unstable (Figure 13 b). The extensions of the meanders propagate along latitude lines and form zonal jets similar to the ones observed in the North Pacific (Figure 13 c). Eventually, the source is stopped and the flow is allowed to decay. After many rotations or tank "days" the westward flow forms zonal jets (Figure 13 d). The streaks of magenta color indicate the eastward jets while the blue color shows the westward jets. Figure 14 shows one azimuthal velocity profile of the jets in the laboratory flow. The velocities are alternating in orientation, from positive to negative, clearly showing that they are alternating jets. It is also interesting to compare the flows at the eastern boundary (right-hand side of the barrier) and the western boundary (left-hand side of the barrier). It is clear that the perturbations do not propagate eastward from the western boundary and the coastal current remains attached to the boundary.

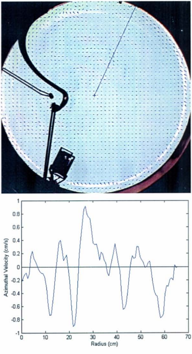

Figure 14: The azimuthal velocity profile was taken from 16Jan09 Exp#2 along the blue line in the image of the tank. The time is the same as in Figure 13 (d), at 303 days, and shows the surface geostrophic velocity.

3.4 Midlatitude Linear Source

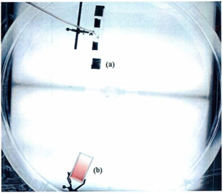

Figure 15: Midlatitude linear source experimental set-up. The source is placed at the bottom of the tank and is a rectangular piece of plexiglass with a slit (a) and the cuvette (b). The source fluid will enter the tank from the right side of the source.

This experimental set-up used a long rectangle source that was placed at the bottom of the tank and ran along the midlatitude regions. In the first experiment the source fluid was fresh water and the tank had a salinity of 20‰ and in the second experiment the salinities were reversed. The main features of the flow are very similar to those of the flow induced by a jet along the barrier discussed previously. Direct observations of typical scales of jets and vortices indicate that baroclinic instability still remains the main mechanism in the initial scale selection (Figure 16 a). The flow develops as a plume propagating westward with an abundance of eddies and meandering jets (Figure 16 b, c). The linear barotropic Rossby waves responsible for the formation of the plume can be seen as wide bands of magenta and blue extending to the west of the baroclinic meanders. Note that AIV imagery allows us to see features that would be difficult or even impossible to observe by other experimental methods. During the final stages of the experiment when the source is switched off the eddy activity subsides but the jets persist in the flow (Figure 16 d).

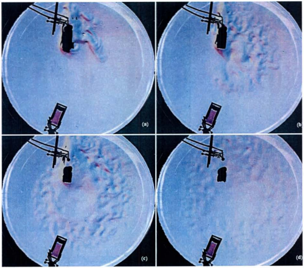

Figure 16: Development of the flow during experiment #1 on January 23, 2009. (a) 198 days [t=11 min], (b) 252 days [t=14 min], (c) 342 days [t=19 min], (d) 468 days [t=26 min].

The vortices observed in the plume do not have a very long life span (typically 3-7 rotations or laboratory days) some of them were tracked from frame to frame in the video. A MATLAB script was written to measure the displacement of individual vortices between consecutive frames (see Appendix B). The average translation speed U_{trans} was measured from the images by marking the center of the vortex in consecutive frames and measuring the displacement between the two points (Figure 17). Since the time difference between frames is known the translation speed was calculated.

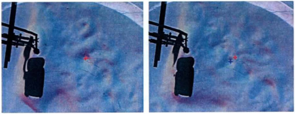

Figure 17: Cropped image of 23Jan09 Experiment #1 frame 29 (left) and frame 30 (right). The red marker indicates the center of the eddy in its initial position and the blue marker indicates the final position of the center of the vortex.

Vortices are identified visually in images of the experimental flow. Vortices are distinct because they are small, circular, concentrations of colour that reflect each colour on the colour slide due to their convex shape. They are easily identified in images of the geostrophic velocity, shown below (Figure 18).

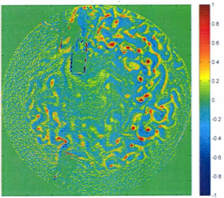

Figure 18: This figure shows the relative vorticity. The vortices are red in colour. The relative vorticity is normalized by the Coriolis parameter f_0. The scale of the surface elevation is in cm.

The diameter of the tracked vortices was measured by a separate MATLAB script (see Appendix B). The measured vortex diameters are larger by a factor of 3-6 when compared to the theoretical Rossby radius of deformation for these experiments which has a value of 2.3 cm (see Tables 4, 8 and 9 in Appendix A). Although the variation of eddy diameter is significant in these experiments the results agree with the typical size of meanders of baroclinically unstable currents measured in these experiments and by previous authors (Blokhina and Afanasyev, 2003). While measuring the vortex diameter, velocity transects of the vortices were plotted and the maximum rotational velocity of the vortices was recorded (Figure 19).

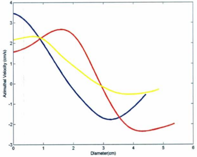

Figure 19: The top image shows the geostrophic velocity image from 23Jan09 Exp#1 at 352 days [t = 19 min 34 s]. The bottom image shows the velocity profiles of the three vortices.

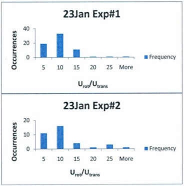

Figure 20: Histogram of the ratio of eddy rotational speed to eddy translation speed. The results demonstrate the nonlinearity of the eddies.

The average rotation velocity U_{rot} of the vortices can be compared to their U_{trans} to demonstrate their nonlinearity. This ratio demonstrates eddy nonlinearity because it compares the fluid velocity to the baroclinic wave speed, which compares nonlinear advection to linear effects (due to Rossby waves) (Chelton et al., 2006). These two terms can be seen in the Navier-Stokes equation for an incompressible fluid, $\rho\left(\frac{\partial u}{\partial t} + u \cdot \nabla u\right) = -\nabla p + \mu \cdot \nabla^2 u$, where $\partial u/\partial t$ is the linear term which has to be taken into account when solving for Rossby waves while $u \cdot \nabla u$ is the nonlinear term which in particular describes the effect of advection. The dynamics are nonlinear when the ratio U_{rot}/U_{trans} exceeds unity; experimental values were within the range of 5 to 8 (Figure 20). The nonlinearity parameter for our experiments was somewhat higher than those described by Chelton et al. (2007) for oceanic eddies for which the ratio was between 1 and 4.

3.5 Analysis

The analysis performed using the images and videos of the experiments captured by the AIV and Thickness methods are described herein. The results of the measurements and the parameters that were calculated are summarized in Appendix A. Several different MATLAB scripts were written to take measurements and analyse the experiments and these are included in Appendix B. In this section the analysis of the experiments will be described. This includes the calculation of control parameters that can be used to make a quantitative comparison of the experimental flows to observed oceanic flows (from Chelton et al., 2006). Some of these control parameters include the Rossby radius of deformation, the Rossby number, the Rhines scale, and the Burger number.

Rossby wave speed

The experimental Rossby wave speed, c, was compared to the theoretical long Rossby wave speed, c_R. The experimental Rossby wave speed is obtained by measuring the propagation of the injected fluid in the videos of the experiments. The fastest waves in our tank are those with the lowest value of $a_{01} = 2.4$ in the dispersion relation (1.10)

$$\omega = \frac{2m\gamma f_0}{\frac{\alpha_{mn}^2}{R^2} + \frac{f_0^2}{gH_0}}$$

Recall that α_{mn} is the n^{th} root of the Bessel function of the m^{th} order, f_0 is the Coriolis parameter, γ is the parameter for the polar β-plane, R is the radius of the tank, g is gravitational acceleration, and H_0 is the depth of water in the tank in the absence of rotation. The dispersion relation can be used to determine the theoretical Rossby speed

$$c_R = \left(\frac{\omega}{m}\right)_{max} = \frac{2\gamma f_0}{\frac{\alpha_{01}^2}{R^2} + \frac{1}{R_d}}$$

The hypothesis that linear Rossby waves provide the underlying mechanism for the propagation of the plumes can be verified by measuring the velocity of the propagation of the front of the plume. In most experiments the propagation speed of the source fluid was easily calculated using the videos of the flow. The propagation speed of the injected fluid was measured by recording the frame number when the red dyed fluid reached the lines A, B, and C, that are 90 degrees apart (Figure 21).

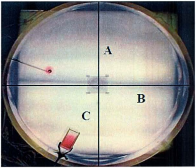

Figure 21: Image of the tank showing the locations of lines A, B, and C. The frame number was recorded when the red source fluid reached each point.

The geometry of the tank is known so the azimuthal distance between each point was calculated and then the speed of the plume was calculated using the time differences. The values of measurements can be found in Tables 4 and 5 in Appendix A. In a few experiments the propagation of the source fluid could not be measured because time stamps were missing or because the injected red source fluid could not be tracked in a tank that already contained red dye. These experiments are 19Jan Exp#1 and Exp#3, 21Jan Exp#1, and 22Jan Exp#1.

The comparison of c and c_R in Figure 22 shows reasonable agreement. When the values of c_R are smaller than 0.015 rad/s there is less agreement and this is likely due to the presence of other dynamics in the experimental flow. The plot suggests that the initial development of the plume is primarily a linear process that provides the deformation field for the development of nonlinear features such as eddies and jets. In these experiments the long baroclinic Rossby wave speed corresponds to the eddy propagation speed.

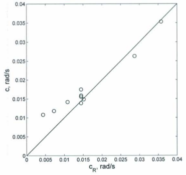

Figure 22: The angular speed of the westward propagation of the plume versus the Rossby speed for the experiments with different values of the baroclinic radius of deformation, R_d.

The Rossby radius of deformation, R_d

The barotropic and baroclinic Rossby radius of deformation was calculated for each experiment. The barotropic Rossby radius of deformation was calculated using $R_d = (gH_0)^2/f_0$ and the baroclinic radius of deformation was calculated using equation (1.13). The calculated values for the single and two-layer experiments are shown in Table 4 and Table 5, respectively. The average barotropic R_d is 18 cm for the single-layer and two-layer experiments. The average baroclinic R_d is 2.6 cm for the single-layer experiments and is 1.2 cm for the two-layer experiments. As mentioned in the theoretical background, the Rossby radius of deformation accounts for the stratification of the baroclinic flow and is the scale for which the relative vorticity and the surface height make equal contributions to the potential vorticity (Pedlosky, 1987). The average eddy diameter measured in the third set of experiments is 7.2 cm, which is larger but the baroclinic R_d by a factor of 3.

The Rossby number, Ro

The Rossby number $Ro = U/f_0L$ measures the influence of background rotation on fluid motion with a characteristic length scale L=32 cm for the experiments shown here and a horizontal velocity scale, U. The value of L is approximately half of the tank radius and is a characteristic scale for the experimental flows. Typical values of the Rossby number, displayed in Table 4 Appendix A, range from 0.002-0.01 which is comparable to results from Chelton et al. (2006) who analysed altimeter data to investigate the dynamical characteristics of the observed eddy-like variability in the Pacific Ocean. Their analysis gave Rossby numbers in the range of 0.001-0.01 indicating that the laboratory experiments correctly model typical oceanic flows in this respect.

The Rhines scale, L_R

When there is small scale turbulence, the Rhines scale $L_R = \sqrt{U_{rms}/\beta}$ gives the distance between the jets. The range of U_{rms} from these experiments is 0.5-1 cm s^{-1} (see Table 4 & 5 in Appendix A). A Matlab script was written to acquire experimental values of U_{rms}. The script generates an image of the geostrophic velocity then prompts the user to select a square section of the tank, crops the image, then allows the user to select eight random points. For each value of U_{rms} two separate images of the flow when zonal jets were present was used. The velocity field is stationary in each image. From each image five cropped sections of the tank were selected to cover most of the surface area of the tank. From each cropped section eight points were selected so the average value of U_{rms} from each experiment comes from 80 separate points in two separate images. The script calculated values of U_{rms} at each of the selected points using the x- and y-components of the geostrophic velocity at each point. The average U_{rms} for the experiment was obtained and then used to calculate L_R. It was found that L_R has a range of 10-20 cm, which is larger than the measured wavelength of the jets. The measured wavelength of the jets was smaller than predicted due to the dynamics of the flow.

Stratification

A useful measure of the stratification is given by the Burger number

$$S = g\frac{\Delta\rho}{\rho}\frac{H}{4\Omega^2 L^2}$$

Where g is the acceleration due to gravity, $\Delta\rho/\rho$ is a characteristic density difference ratio for the fluid over its vertical scale of motion H, which is the initial depth of the fluid in the tank, Ω is the rotation rate of the tank, and L is the horizontal length scale (Pedlosky, 1987). This parameter can also be written in terms of the ratio of length scales,

$$S = \left(\frac{R_d}{L}\right)^2$$

For this tank we selected L=32 cm with a baroclinic R_d that ranges from 2-3 cm giving S = 0.0039-0.0089. The value of L was selected because it's about half of the radius of the tank. The Burger number can be used to compare the Rossby radius of deformation in our experiments to that in a typical ocean flow in the Pacific. Using a length scale for the Pacific Ocean of 10000 km and using R_d ranging from 20 km at 40 degrees latitude to 230 km near the equator (Chelton et al., 1998) the Burger number ranges from $4\text{x}10^{-6}$ to $5\text{x } 10^{-4}$. See Tables 4 and 5 in Appendix A for all the calculated experimental values.

Barotropic Instability

The baroclinic instability is clearly present in the flow due to the dynamics of the injected fluid interacting with the tank fluid. To demonstrate that barotropic instability is present, a plot was created that shows the azimuthal velocity profile and the value of the expression β - U_{rr} (Figure 23). This expression represents the Rayleigh–Kuo inflection point criterion of barotropic instability (Vallis, 2006). The profile shows that β - U_{rr} changes sign in the narrowest jets indicating that these jets are potentially unstable with respect to barotropic instability.

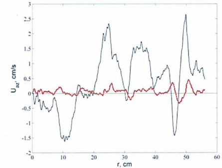

Figure 23: The vertical axis is azimuthal velocity in cm/s while the horizontal axis is radial distance in cm. The profile of the azimuthal velocity is the black line while the red line shows β - U_{rr}. The azimuthal velocity crosses the zero-line which demonstrates that the jets have alternating velocity.

3.6 Conclusion

In this thesis the mechanisms involved in the formation of zonal jets were investigated in an experimental setting. Three different flow configurations were studied in a circular tank filled with saline fluid that was installed on a rotating table. The circular tank was rotated in an anticlockwise direction and effectively models northern hemisphere dynamics on a polar β-plane. A buoyancy source injects fluid into the tank to create the experimental flows that demonstrate barotropic and baroclinic instability, the creation of β-plumes, and the formation of zonal jets.

The first experimental set-up with a mid-latitude point source was designed to demonstrate a simple β-plume model. The second experimental set-up had an eastern boundary and a fluid source at the surface of the water and was intended to demonstrate the development of zonal jets from β-plumes created by baroclinic instability of an eastern boundary current. The third experimental set-up had a midlatitude linear source and was designed to demonstrate the main features of a β-plume and avoid the preset length scale of plumes that would be controlled by the size of the coastal meanders as in the barrier experiment. This experiment was also meant to demonstrate the formation of zonal jets and to investigate the possible role of nonlinear eddies in zonal jet formation. These experiments demonstrate several processes including the development of β-plumes from perturbations created by a coastal current at an eastern boundary; the formation of zonal jets by linear mechanisms; and the contributions of nonlinear eddies to the structure of the jets. The experiments also show that barotropic instability plays an important role in the dynamics of the experimental flows.

The first set of laboratory experiments shows the formation of discrete anticyclonic eddies. The second set of laboratory experiments described clearly demonstrates the process of the development of β-plumes from perturbations at the eastern boundary. The development of β-plumes from perturbations at an eastern boundary is difficult to observe in the ocean because only the result of the flow evolution can be observed in those studies rather than a development of the flow from initial conditions. In these experiments the observed jets formed as a result of the linear development of β-plumes. The source injected the red fluid into the tank where the radial boundary meets the tank wall and created an eastern boundary current. The baroclinic instability of the eastern boundary current, visible in the form of meanders, created β-plumes that began to propagate to the west. Each β-plume consisted of an eastward and westward jet along its Northern and Southern flanks. This mechanism leading to the formation of zonal jets supports the hypothesis presented by Centurioni et al. (2008). The initial propagation of the plume front was governed by westward propagating long Rossby waves and the developing plume showed an abundance of vortices. The vortices demonstrate a significant nonlinearity and are the product of the baroclinic instability with their length scale related to the baroclinic Rossby radius of deformation.

In the third set of experiments with the source extending in the radial direction the interactions of eddies and jets were observed. The experiments showed that barotropic linear Rossby waves are responsible for the formation of the plume. The eddies are probably the product of baroclinic instability with their length scale related to the baroclinic Rossby radius of deformation. Nonlinear eddies were also found to have a significant effect on the flow and this was shown by comparing the eddy translation speed to the eddy rotation speed.

The experimental flows provided a sufficient model of the oceanic flows, demonstrated the formation of zonal jets from β-plumes, showed that zonal jets are real and remain after time averaging and are not the result of averaging the tracks of eddies, and also show that both linear and nonlinear mechanisms are involved in the formation of zonal jets.

References

Afanasyev, Y.D., and J.Wells, (2005), Quasi-two-dimensional turbulence on the polar beta-plane: Laboratory experiments, Geophysical and Astrophysical Fluid Dynamics, 99 (1), 1-17.

Afanasyev, Y.D., P.B. Rhines, E.G. Lindahl, (2006), Emission of Inertial Waves by Baroclinically Unstable Flows: Laboratory Experiments with Altimetric Imaging Velocimetry, J. Atmos. Sci., 65, 250-262 DOI 10.1175/2007JAS2336.1.

Afanasyev, Y.D., P.B. Rhines, E.G. Lindahl, (2009), Velocity and potential vorticity fields measured by altimetric imaging velocimetry in the rotating fluid, Exp. Fluids, DOI 10.1007/s00348-009-0689-3.

Afanasyev, Y.D., S. O'Leary, P.B. Rhines, E.G. Lindahl (2010), On the origin of jets in the ocean, Geophysical & Astrophysical Fluid Dynamics, Submitted for review: Sept. 2010.

Arfken G.B. and Weber H.J., Mathematical Methods for Physicists 5th edition, 2001. (Harcourt/Academic Press: Burlington).

Balmforth, N.J., S.G. Llewellyn Smith, and W.R. Young, (1998), Dynamics of interfaces and layers in a stratified turbulent fluid, J. Fluid Mech., 355, 389-358.

Berloff, P., I. Kamenkovich, and J. Pedlosky, (2009), A Mechanism of Formation of Multiple Zonal Jet in the Oceans, J. Fluid Mechanics, 628, 395-425, DOI:10.1017/S0022112009006375.

Blokhina, M. D., and Y. D. Afanasyev (2003), Baroclinic instability and transient features of mesoscale surface circulation in the Black Sea: laboratory experiment, J. Geophys. Res., 108 (C10), 3322, doi:10.1029/3003JC001979.

Centurioni, L.R., J.C. Ohlmann, and P.P. Niiler, (2008), Permanent meanders in the California Current System, J. Phys. Oceanogr., 38, 1690-1710.

Chelton, D.B., and M.G. Schlax (1996), Global observations of oceanic Rossby waves, Science, 72, 234-238.

Chelton, D.B., R.A. deSzoeke, M.G. Schlax, K El Naggar and N. Siwertz (1998), Geographical variability of the first-baroclinic Rossby radius of deformatio,. J. Phys. Oceanogr., 28, 433-460.

Chelton, D.B., M.G. Schlax, R.M. Samelson, and R.A. de Szoeke (2006), Global observations of westward energy propagation in the ocean: Rossby waves or nonlinear eddies?, AGU Fall Meeting, San Franciso, CA.

Chelton, D.B., M.G. Schlax, R.M. Samelson, and R.A. de Szoeke (2007), Global observations of large oceanic eddies, Geophys. Res. Lett., 34, L15606.

Chelton, D.B., and M.G. Schlax (2008), The influence of mesoscale eddies on the detection of quasi-zonal jets in the ocean, Geophys. Res. Lett.,DOI: 10.1029.

Danilov, S., and D. Gurarie, (2000), Quasi-two-dimensional turbulence, Physics, 43 (9), 863-900.

Davey, M. K., Killworth, P. D. (1989), Flows produced by discrete sources of buoyancy, J. Phys. Ocean. 19, 1279-1290.

Derzho, O.G., Y.D. Afanasyev (2008), Rotating dipolar gyres on a γ-plane, Physics of Fluids, 20, 036603.

Galperin, B., H. Nakano, T. P. Huang, and S. Sukoriansky (2004), The ubiquitous zonal jets in the atmospheres of giant planets and Earth's oceans, Geophys. Res. Lett., 31, L13303, doi:10.1029/2004GL019691.

Galperin, B., S. Sukoriansky, N. Dikovskaya, P. L. Read, Y. H. Yamazaki, and R. Wordsworth, (2006), Anisotropic turbulence and zonal jets in rotating flows with a β-effect, Nonlinear Processes in Geophysics, 13, 83-98.

Galperin, B., S. Sukoriansky, N. Dikovskaya (2010), Geophysical flows with anisotropic turbulence and dispersive waves: Flows with a β-effect, Ocean Dynamics, 60 (2), 427-441, DOI: 10.1007/s10236-010-0278-2.

Gill, A. E., (1982), Atmosphere-Ocean Dynamics, Academic Press, San Diego, Volume 30.

Hristova, H.G., J. Pedlosky, and M. A. Spall (2008), Radiating Instability of a Meridional Boundary Current, J. Phys. Oceanogr., 38, 2294-2307.

Kelly, K.A., R.C. Beardsley, R. Limeburner, and K.H. Brink (1998), Variability of the near-surface eddy kinetic energy in the California Current based on altimetric, drifter, and moored current data, J. of Geophys. Res., 103(C6), 13067-13083.

Kundu, P.K., I. M. Cohen, (1987), Fluid Mechanics, Academic Press, San Diego, 2nd edition.

Masumoto, Y., et al. (2004), A fifty-year eddy-resolving simulation of the world ocean - Preliminary outcomes of OFES (OGCM for the Earth Simulator), J. Earth Simulator, 1, 35-36.

Mathworks Incorporated, (1994-2011), Matlab – The Language of Technical Computing, Software.

Maximenko, N.A., M. Bang, and H. Sasaki, (2005), Observational evidence of alternating zonal jets in the world ocean, Geophys. Res. Lett., 32, L12607.

Maximenko, N.A., O.V. Melnichenkio, P.P Niiler, and H. Sasaki (2008), Stationary mesoscale jet-like features in the ocean, Geophys. Res. Lett., 35, L08603.

Melnichenko, O.V., N.A. Maximenko, N. Schneider, H. Sasaki (2010), Quasi-stationary striations in basin-scale oceanic circulation: vorticity balance from observations and eddy-resolving model, Ocean Dynamics, DOI:10.1007/s10236-009-0260-z.

Nakano, H., and H. Hasumi (2005), A series of zonal jets embedded in the broad zonal flows in the Pacific obtained in eddy-permitting ocean general circulation models, J. Phys. Oceanogr., 35 (4), 474-488.

Nadiga, B. T., (2006), On zonal jets in oceans, Geophys. Res. Lett., 33, L10601.

Niiler, P.P., N.A. Maximenko, G.G. Panteleev, T. Yamagata, and D.B.Olson (2003), Near-surface dynamical structure of the Kuroshio Extension, J. of Geophys. Res., 108(C6), 3193, doi:10.1029/2002JC001461.

Pedlosky, J. (1987), Geophysical Fluid Dynamics, Springer-Verlag, New York, 2nd edition.

Pedlosky, J. (1992), The Baroclinic Structure of the Abyssal Circulation, J. Phys. Oceanogr., 22, 652-659.

Pedlosky, J. (1996), Ocean Circulation Theory, Springer, New York.

Rhines, P.B. (1975), Waves and turbulence on a beta-plane, J. Fluid Mechanics, 69 (3), 417-443.

Rhines, P.B. (1994), Jets, Chaos, 4, 313.

Rhines, P.B. (2007), Jets and Orography: Idealized Experiments with Tip-Jets and Lighthill Blocking, J. Atmos. Sci., 64, 3627-3639.

Richards, K. J., N. A. Maximenko, F. O. Bryan, and H. Sasaki (2006), Zonal jets in the Pacific Ocean, Geophys. Res. Lett., 33, L03605, doi:10.1029/2005GL024645.

Schlax, M.G., and D.B. Chelton (2008), The Influence of Mesoscale Eddies on the Detection of Quasi-Zonal Jets in the Ocean, Geophys. Res. Lett., DOI:10.1029.

Scott, R.B., B.K. Arbic, C.L. Holland, A. Sen, B. Qiu (2008), Zonal versus meridional velocity variance in satellite observations and realistic and idealized ocean circulation models, Ocean Modelling, 23, 102-112, DOI:10.1016/j.ocemod.2008.04.009.

Spall, M. A. (2001), Large-Scale Circulation Forced by Localized Mixing over a Sloping Bottom, J. Phys. Oceanogr., 31, 2369-2384.

Spall, M. A., Pickart, R. S. (2003), Wind-Driven Recirculations and Exchange in the Labrador and Irminger Seas, J. Phys. Oceanogr., 33, 1829-1845.

Stewart, R. H., (2005), Introduction to Physical Oceanography, Chapter 8, http://oceanworld.tamu.edu/resources/ocng_textbook/chapter08/chapter08_04.htm.

Stommel, H.M., (1982), Is the South Pacific helium-3 plume dynamically active? Earth Planet. Sci. Lett., 61, 63-67.

Vallis, G. K., (2006), Atmospheric and Oceanic Fluid Dynamics: Fundamentals and Large-Scale Circulation, Cambridge University Press, New York.

Appendix A

Table 1: List of Experiments.

Date	**12-Jan-09**								
Exp #	**Ω (rad/s)**	**Layer**	**Tank Salinity (‰)**	**Height (cm)**	**Source Salinity (‰)**	**Source**	**Source Location**	**Barrier**	**Camera**
1	1.919	One	Freshwater	8	25	circle	Tank bottom	Yes	Sony
2	1.919	One	Freshwater	8	25	circle	Tank bottom	Yes	Sony
3	1.919	One	Freshwater	8	6.25	circle	Tank bottom	Yes	Sony
Date	**14-Jan-09**								
Exp #	**Ω (rad/s)**	**Layer**	**Tank Salinity (‰)**	**Height (cm)**	**Source Salinity (‰)**	**Source**	**Source Location**	**Barrier**	**Camera**
1	1.919	Two	12 (bottom); freshwater (top)	5 (bottom); 12 (top)	12	circle	3cm above bottom	No	Sony
Date	**15-Jan-09**								
Exp #	**Ω (rad/s)**	**Layer**	**Tank Salinity (‰)**	**Height (cm)**	**Source Salinity (‰)**	**Source**	**Source Location**	**Barrier**	**Camera**
1	1.834	Two	8 (bottom); freshwater (top)	4 (bottom); 8 (top)	8	circle	3cm above bottom	No	Sony
2	1.922	One	2	12	8	circle	Tank bottom	No	Sony
Date	**16-Jan-09**								
Exp #	**Ω (rad/s)**	**Layer**	**Tank Salinity (‰)**	**Height (cm)**	**Source Salinity (‰)**	**Source**	**Source Location**	**Barrier**	**Camera**
1	1.894	One	30	6	Freshwater	wedge	Water surface	Yes	Sony
2	1.894	One	15	6	Freshwater	wedge	Water surface	Yes	Sony
3	1.894	One	50	6	Freshwater	wedge	Water surface	Yes	Sony
Date	**18-Jan-09**								
Exp #	**Ω (rad/s)**	**Layer**	**Tank Salinity (‰)**	**Height (cm)**	**Source Salinity (‰)**	**Source**	**Source Location**	**Barrier**	**Camera**
1	1.894	One	25	6	Freshwater	wedge	Water surface	Yes	Sony
2	1.894	One	21	6	Freshwater	wedge	Water surface	Yes	Sony

Table 1: List of Experiments. (continued)

Date	19-Jan-09								
Exp #	Ω (rad/s)	Layer	Tank Salinity (‰)	Height (cm)	Source Salinity (‰)	Source	Source Location	Barrier	Camera
1	1.894	One	20	6	Freshwater	wedge	Water surface	Yes	Sony
2	1.894	One	20	6	Freshwater	wedge	Water surface	Yes	Sony
3	1.894	One	19	6	Freshwater	wedge	Water surface	Yes	Sony
4	1.894	One	22	6	Freshwater	circle	3cm above bottom	No	Sony
5	1.894	One	20	5.5	Freshwater	circle	4cm above bottom	No	Sony
6	1.894	One	Freshwater	5	23	wedge	Tank bottom	No	Sony
7	1.894	One	Freshwater	5	23	wedge	Tank bottom	Yes	Sony
Date	20-Jan-09								
Exp #	Ω (rad/s)	Layer	Tank Salinity (‰)	Height (cm)	Source Salinity (‰)	Source	Source Location	Barrier	Camera
1	1.894	One	Freshwater	5	20	linear	Tank bottom	No	Sony
2	1.894	One	Freshwater	5.5	40	linear	Tank bottom	No	Sony
Date	21-Jan-09								
Exp #	Ω (rad/s)	Layer	Tank Salinity (‰)	Height (cm)	Source Salinity (‰)	Source	Source Location	Barrier	Camera
1	1.896	Two	Freshwater (bottom); 30 (top)	2 (bottom); 5 (top)	30	linear	Tank bottom	No	Sony
2	1.894	One	Freshwater	5.5	10	linear	Tank bottom	No	Sony
Date	22-Jan-09								
Exp #	Ω (rad/s)	Layer	Tank Salinity (‰)	Height (cm)	Source Salinity (‰)	Source	Source Location	Barrier	Camera
1	1.894	Two	30 (bottom); Freshwater (top)	5 (bottom); 2 (top)	30	linear	Tank bottom	No	Sony
Date	23-Jan-09								
Exp #	Ω (rad/s)	Layer	Tank Salinity (‰)	Height (cm)	Source Salinity (‰)	Source	Source Location	Barrier	Camera
1	1.894	One	20	5	Freshwater	linear	2cm above bottom	No	Aptina
2	1.894	One	Freshwater	5	20	linear	Tank bottom	No	Aptina

Table 2: Experiment Constants.

Tank Rotation Rate (rad/s)	1.89
Coriolis parameter (f=2Ω)	3.79
Gravity (cm/s^2)	981.00
Freshwater density (kg/m^3)	998.21
Temperature (°C)	20.00
r_o (cm)	32.00
Tank Radius	65.00
Gravity (cm/s^2)	980.67

Table 3: Source Volume Flow Rate.
Mass flow rate = 14.9 g/s

Video File	Source Density (kg/m^3)	Source Density (g/cm^3)	Volume Flow Rate (L/s)
12Jan 1	1017.18	1.017	0.015
12Jan 2	1017.18	1.017	0.015
12Jan 3	1002.98	1.003	0.015
14Jan 1	1007.31	1.007	0.015
15Jan 1	1004.28	1.004	0.015
15Jan 2	1004.28	1.004	0.015
16Jan 1	998.23	0.998	0.015
16Jan 2	998.23	0.998	0.015
16Jan 3	998.23	0.998	0.015
18Jan 1	998.23	0.998	0.015
18Jan 2	998.23	0.998	0.015
19Jan 1	998.23	0.998	0.015
19Jan 2	998.23	0.998	0.015
19Jan 3	998.23	0.998	0.015
19Jan 4	998.23	0.998	0.015
19Jan 5	998.23	0.998	0.015
19Jan 6	1015.66	1.016	0.015
19Jan 7	1015.66	1.016	0.015
20Jan 1	1013.39	1.013	0.015
20Jan 2	1028.61	1.029	0.014
21Jan 1	1020.95	1.021	0.015
21Jan 2	1005.82	1.006	0.015
22Jan 1	1020.95	1.021	0.015
23Jan 1	998.23	0.998	0.015
23Jan 2	1013.39	1.013	0.015

Table 4: Single-Layer Experiments.

	H_o (cm)	Barot R_d (cm)	Baroc R_d (cm)	h (cm)	β ($cm^{-1}\ s^{-1}$)	U_{barocl}= β*R_d^2 (cm/s)	V_{azi} (rad/s)	Layer thick (cm)	U_{rms} (cm/s)	L_R (cm)	L_R/D	Ro=U/fL	$U/\beta L^2$	Fr=U/fR_d	S= $g(\Delta\rho/\rho)$* $(H/4\Omega^2L^2)$
12Jan 1	8	---	3.22	6.01	0.0738	0.766	---	---	---	---	---	---	---	---	---
12Jan 2	8	23.4	3.22	6.01	0.0738	0.766	---	---	---	---	---	---	---	---	---
12Jan 3	8	23.4	1.61	6.01	0.0738	0.192	---	---	---	---	---	---	---	---	---
15Jan 2	12	23.4	0.19	10.01	0.0443	0.002	0.0108	0.77	0.65	35.3	0.27	0.0054	0.0143	0.0891	0.0036
16Jan 1	6	---	3.02	4.01	0.1106	1.010	0.0896	1.47	0.96	28.3	0.22	0.0079	0.0085	0.0838	0.0089
16Jan 2	6		2.15	4.01	0.1106	0.511	0.1014	0.90	0.39	18.1	0.14	0.0032	0.0035	0.0483	0.0045
16Jan 3	6	---	3.88	4.01	0.1106	1.665	0.0887	1.20	0.34	17.0	0.13	0.0028	0.0030	0.0234	0.0147
18Jan 1	6	20.3	2.76	4.01	0.1106	0.845	---	---	---	---	---	---	---	---	---
18Jan 2	6	20.3	2.54	4.01	0.1106	0.712	0.0753	1.12	0.30	15.7	0.12	0.0024	0.0026	0.0307	0.0063
19Jan 1	6	20.3	2.48	4.01	0.1106	0.678	---	---	---	---	---	---	---	---	---
19Jan 2	6	---	2.48	4.01	0.1106	0.678	0.0807	0.56	0.53	21.3	0.16	0.0044	0.0047	0.0565	0.0060
19Jan 3	6	20.3	2.41	4.01	0.1106	0.645	---	---	---	---	---	---	---	---	---
19Jan 4	6	20.3	2.60	4.01	0.1106	0.745	0.0311	0.50	0.96	29.1	0.22	0.0079	0.0085	0.0976	0.0066
19Jan 5	5.5	---	2.37	3.51	0.1264	0.710	0.0369	0.45	0.71	24.4	0.19	0.0058	0.0054	0.0785	0.0055
19Jan 6	5	20.3	2.44	3.01	0.1474	0.879	0.0265	0.94	1.12	31.5	0.24	0.0092	0.0074	0.1210	0.0058
19Jan 7	5	20.3	2.44	3.01	0.1474	0.879	0.0128	1.01	0.51	18.9	0.15	0.0042	0.0034	0.0551	0.0058
20Jan 1	5	20.3	2.28	3.01	0.1474	0.764	0.0139	1.03	0.37	14.9	0.11	0.0030	0.0024	0.0423	0.0051
20Jan 2	5.5	20.3	3.38	3.51	0.1264	1.445	0.0169	0.74	0.71	22.4	0.17	0.0059	0.0055	0.0554	0.0112
21Jan 2	5.5	19.4	1.69	3.51	0.1264	0.361	---	---	---	---	---	---	---	---	---
23Jan 1	5	18.5	2.26	3.01	0.1474	0.753	0.0203	1.25	0.60	14.1	0.11	0.0049	0.0040	0.0701	0.0050
23Jan 2	5	18.5	2.28	3.01	0.1474	0.764	0.0159	0.40	0.58	11.0	0.08	0.0048	0.0038	0.0672	0.0051

Table 5: Two-Layer Experiments.

	Layer	$\Delta\rho$ (kg/m^3)	H_o (cm)	Barot R_d (cm)	Baroc R_d (cm)	V_{azi} (rad/s)	h (cm)	β ($cm^{-1}\ s^{-1}$)	$U_{baroc}= \beta * R_d^2$ (cm/s)
14Jan	lower	0.03	5	18.5	0.096		3.0	0.147	0.001
1	upper	9.13	12	28.6	2.73	0.019	10.0	0.044	0.332
15Jan	lower	6.10	4	16.5	1.28		2.0	0.221	0.366
1	upper	0.00	8	23.4	0.000	0.018	6.0	0.074	0.000
21Jan	lower	0.00	2	11.7	0.000		0.0	45.075	0.000
1	upper	22.77	5	18.5	2.76	0.093	3.0	0.147	1.123

	Layer thick (cm)	U_{rms} (cm/s)	L_R (cm)	$Ro=U/fL$	$U/\beta L^2$	$Fr=U/f R_d$	$S=g(\Delta\rho/\rho)*(H/4\Omega^2 L^2)$
14Jan	---	---	---	---	---	---	0.0000
1	0.80	0.33	12.3	0.0027	0.0072	0.0313	0.0073
15Jan	---	---	---	---	---	---	0.0016
1	1.44	0.19	14.7	0.0016	0.0025	---	0.0000
21Jan	---	---	---	---	---	---	0.0000
1	1.18	0.47	14.5	0.0039	0.0031	0.0449	0.0074

Table 6: Comparison of Baroclininc R_d to Source Velocity for Single-Layer Experiments.

Experiment	R_d (cm)	V_{azi} (rad/s)	Source location in fluid layer (surface or bottom)
15Jan #2	1.93	0.0108	Bottom
16Jan #1	3.02	0.0896	Surface
16Jan #2	2.15	0.1014	Surface
16Jan #3	3.88	0.0887	Surface
18Jan #2	2.54	0.0753	Surface
19Jan #2	2.48	0.0807	Surface
19Jan #4	2.60	0.0311	Bottom
19Jan #5	2.37	0.0369	Bottom
19Jan #6	2.44	0.0265	Bottom
19Jan #7	2.44	0.0128	Bottom
20Jan #1	2.28	0.0139	Bottom
20Jan #2	3.38	0.0169	Bottom
21Jan #2	1.69	0.0118	Bottom
23Jan #1	2.26	0.0203	Bottom
23Jan #2	2.26	0.0159	Bottom
23Jan #3	2.28	0.0156	Bottom

Table 7: Rossby number for Single-Layer Experiments

Experiment	$Ro = U/fL$
15Jan Exp#2	0.0054
16Jan Exp#1	0.0079
16Jan Exp#2	0.0032
16Jan Exp#3	0.0028
18Jan Exp#2	0.0024
19Jan Exp#2	0.0044
19Jan Exp#4	0.0079
19Jan Exp#5	0.0058
19Jan Exp#6	0.0092
19Jan Exp#7	0.0042
20Jan Exp#1	0.0030
20Jan Exp#2	0.0059
23Jan Exp#1	0.0049
23Jan Exp#2	0.0048

Table 8: 23Jan Exp#1 Vortex Diameter & Velocity Measurements.

Experiment Image ID	U_{rot} (cm/s)	U_{trans} (cm/s)	Ratio (U_{rot}/U_{trans})	Vortex Diameter (cm)
F23 Vorx1	2.25	0.21	10.70	2.25
F23 Vorx2	2.40	0.34	7.06	2.40
F23 Vorx3	3.24	0.29	11.17	3.24
F25 Vorx1	1.48	0.21	7.04	1.48
F25 Vorx2	1.88	0.34	5.53	1.88
F25 Vorx3	2.16	0.29	7.45	2.16
F26 Vorx1	2.26	0.55	4.11	2.26
F26 Vorx2	3.20	0.59	5.43	3.20
F26 Vorx3	2.17	0.54	4.01	2.17
F27 Vorx1	1.90	0.55	3.46	1.90
F27 Vorx2	2.37	0.59	4.02	2.37
F27 Vorx3	2.29	0.54	4.24	2.29
F29 Vorx1	2.29	0.19	12.04	2.29
F29 Vorx2	3.33	0.19	17.53	3.33
F29 Vorx3	2.93	0.20	14.66	2.93
F30 Vorx1	2.45	0.19	12.90	2.45
F30 Vorx2	2.42	0.19	12.72	2.42
F30 Vorx3	2.26	0.20	11.32	2.26
F32 Vorx1	2.78	0.79	3.52	4.65
F32 Vorx2	1.02	0.32	3.19	6.31
F32 Vorx3	1.75	0.56	3.13	4.27
F33Vorx1	3.07	0.79	3.89	6.03
F33 Vorx2	2.53	0.32	7.91	6.97
F33 Vorx3	1.72	0.56	3.07	6.98
F35 Vorx1	2.15	0.42	5.12	2.15
F35 Vorx2	3.01	0.69	4.36	3.01
F35 Vorx3	3.10	0.47	6.60	3.10
F36 Vorx1	1.63	0.42	3.89	1.63
F36 Vorx2	2.93	0.69	4.25	2.93
F36 Vorx3	2.73	0.47	5.80	2.73
F43 Vorx1	2.77	0.53	5.23	5.00
F43 Vorx2	2.01	0.31	6.48	5.07
F43 Vorx3	2.55	0.61	4.18	5.04
F44 Vorx1	3.50	0.53	6.60	5.83
F44 Vorx2	2.64	0.31	8.50	6.26
F44 Vorx3	2.89	0.61	4.74	5.83
F46 Vorx1	3.50	0.57	6.15	3.50
F46 Vorx2	2.21	0.26	8.50	2.21
F46 Vorx3	3.07	0.62	4.95	3.07

Table 8: 23Jan Exp#1 Vortex Diameter & Velocity Measurements. (continued)

Experiment Image ID	U_{rot} (cm/s)	U_{trans} (cm/s)	Ratio (U_{rot}/U_{trans})	Vortex Diameter (cm)
F47 Vorx1	4.07	0.57	7.14	4.07
F47 Vorx2	3.15	0.26	12.11	3.15
F47 Vorx3	1.99	0.62	3.20	1.99
F52 Vorx1	3.66	0.37	9.90	8.15
F52 Vorx2	1.46	0.23	6.36	5.82
F52 Vorx3	2.83	0.38	7.44	5.81
F53 Vorx1	2.82	0.37	7.63	5.62
F53 Vorx2	0.98	0.23	4.25	6.78
F53 Vorx3	0.94	0.38	2.47	6.81
F55 Vorx1	2.62	0.32	8.17	2.62
F55 Vorx2	1.76	0.26	6.76	1.76
F55 Vorx3	2.77	0.25	11.09	2.77

Table 9: 23Jan Exp#2 Vortex Diameter & Velocity Measurements..

Experiment Image ID	Max Vortex Velocity (cm/s)	Vortex Speed (cm/s)	Ratio (U_{rot}/U_{trans})	Vortex Diameter (cm)
F13 Vorx1	2.23	0.11	20.31	7.38
F13 Vorx2	1.61	0.13	12.35	8.93
F13 Vorx3	2.32	0.09	25.77	8.93
F15 Vorx1	2.42	0.11	21.98	13.39
F15 Vorx2	2.08	0.13	16.03	7.18
F15 Vorx3	1.81	0.09	20.07	9.62
F21 Vorx1	2.09	0.21	9.94	14.56
F21 Vorx2	1.87	0.31	6.02	11.64
F21 Vorx3	1.28	0.32	3.99	11.72
F23 Vorx1	2.78	0.21	13.26	8.79
F23 Vorx2	2.47	0.31	7.96	16.61
F23 Vorx3	2.33	0.32	7.27	14.36
F23 Vorx1	2.78	0.68	4.09	8.79
F23 Vorx2	2.47	0.54	4.57	16.61
F23 Vorx3	2.33	0.38	6.12	14.36
F24 Vorx1	1.59	0.68	2.34	9.63
F24 Vorx2	2.89	0.54	5.36	10.88
F24 Vorx3	1.36	0.38	3.58	11.30
F26 Vorx1	2.17	0.24	9.05	9.43
F26 Vorx2	2.06	0.32	6.45	11.26
F26 Vorx3	2.41	0.41	5.88	9.06
F27 Vorx1	2.22	0.24	9.26	11.64
F27 Vorx2	1.66	0.32	5.17	8.51
F27 Vorx3	1.77	0.41	4.31	9.40
F27 Vorx1	2.22	0.41	5.42	11.64
F27 Vorx2	1.66	0.22	7.53	8.51
F27 Vorx3	1.77	0.37	4.77	9.40
F28 Vorx1	1.71	0.41	4.18	10.86
F28 Vorx2	1.24	0.22	5.63	5.41
F28 Vorx3	1.73	0.37	4.67	9.51
F34 Vorx1	2.03	0.17	11.94	10.67
F34 Vorx2	1.22	0.25	4.87	11.37
F34 Vorx3	0.99	0.17	5.84	13.46
F35 Vorx1	1.41	0.17	8.32	9.77
F35 Vorx2	1.20	0.25	4.79	10.99
F35 Vorx3	1.92	0.17	11.31	8.17

Appendix B

This appendix contains scripts that were written in Matlab and used to analyse the videos and images of the experiments for this thesis. The name of the file followed by its contents are shown here.

Filename: vortex_soleary.m

```
%%%%%%%%%%%%%%%%%%%%%%%%%%%%%%%%%%%%%%%%%%%%%%%%%%%%%%%%%%%%%%%%%%%%%%%%%%%%%

% This file measures the diameter of selected vortices and plots the
% azimuthal velocity along each selected diameter so that the maximum speed
% inside the vortex can be determined.
% Sheilagh O'Leary, January 2010
% email: soleary@mun.ca
% fname = vortex_soleary
%%%%%%%%%%%%%%%%%%%%%%%%%%%%%%%%%%%%%%%%%%%%%%%%%%%%%%%%%%%%%%%%%%%%%%%%%%%%%

% load previous results
cd (results_dir)
load ([endname_slide experID_calibr])
load(['tank_size_' experID_calibr])
load(['null_velocity_' experID_calibr])
cd (work_dir)
Nframe=1;
% scale in cm/pixel
scale=D/(px(2)-px(1));

%%%%%%%%%%%%%%%%%%%%%%%%%%%%%%%%%%%%%%%%%%%%%%%%%%%%%%%%%%%%%%%%%%%%%%%%%%%%%
% This section (not shown) was copied from main_calibration_29April.m and
% opens the video for analysis.
%%%%%%%%%%%%%%%%%%%%%%%%%%%%%%%%%%%%%%%%%%%%%%%%%%%%%%%%%%%%%%%%%%%%%%%%%%%%%

%%%%%%%%%%%%%%%%%%%%%%%%%%%%%%%%%%%%%%%%%%%%%%%%%%%%%%%%%%%%%%%%%%%%%%%%%%%%%
% This section allows the user to mark the diameter of three vortices in the
% tank and then outputs the measured diameter and velocity profile of the
% marked vortices.
%%%%%%%%%%%%%%%%%%%%%%%%%%%%%%%%%%%%%%%%%%%%%%%%%%%%%%%%%%%%%%%%%%%%%%%%%%%%%
'Select input points to determine vortex diameter & velocity profile'
npp=2; %the number of input points
'Vortex 1'
[lx,ly]=ginput(npp); %input the points
'Vortex 2'
[tx,ty]=ginput(npp);
'Vortex 3'
[bx,by]=ginput(npp);

lx1=lx(1);
ly1=ly(1);
lx2=lx(2);
ly2=ly(2);
tx1=tx(1);
ty1=ty(1);
tx2=tx(2);
```

```
ty2=ty(2);
bx1=bx(1);
by1=by(1);
bx2=bx(2);
by2=by(2);

% mark the vortex diameters
llx=lx;
lly=ly;
line(llx,lly)
ttx=tx;
tty=ty;
line(ttx,tty,'Color','r')
bbx=bx;
bby=by;
line(bbx,bby,'Color','y')

c1=(ly1-ly2)/(lx1-lx2);
c2=((ly2*lx1)-(ly1*lx2))/(lx1-lx2);
c3=(ty1-ty2)/(tx1-tx2);
c4=((ty2*tx1)-(ty1*tx2))/(tx1-tx2);
c5=(by1-by2)/(bx1-bx2);
c6=((by2*bx1)-(by1*bx2))/(bx1-bx2);

stpp1=abs(lx2-lx1)/100;
xline1=min(lx):stpp1:max(lx);
yline1=xline1*c1+c2;
hold on
%repeat
stpp2=abs(tx2-tx1)/100;
xline2=min(tx):stpp2:max(tx);
yline2=xline2*c3+c4;
hold on
stpp3=abs(bx2-bx1)/100;
xline3=min(bx):stpp3:max(bx);
yline3=xline3*c5+c6;
hold on

% distance calculation
% this is distance in cm because it is pixels*scale where scale is cm/pixel
diameter1=(sqrt(((lx2-lx1)^2)+((ly2-ly1)^2)))*scale
diameter2=(sqrt(((tx2-tx1)^2)+((by2-by1)^2)))*scale
diameter3=(sqrt(((tx2-tx1)^2)+((ty2-ty1)^2)))*scale

%create the step
st1=(diameter1/100);
st2=(diameter2/100);
st3=(diameter3/100);
% create a vector for the diameter of the vortex
dd1 = (0:st1:diameter1);
dd2 = (0:st2:diameter2);
dd3 = (0:st3:diameter3);

% Find the azimuthal velocity along the diameter of the vortex.
% this is for calculation of azimuthal velocity.
length_line1=sqrt((lx(1)-lx(2))^2+(ly(1)-ly(2))^2);
```

```
sina1=(ly(1)-ly(2))/length_line1;
cosa1=(lx(2)-lx(1))/length_line1;
% repeat
length_line2=sqrt((tx(1)-tx(2))^2+(ty(1)-ty(2))^2);
sina2=(ty(1)-ty(2))/length_line2;
cosa2=(tx(2)-tx(1))/length_line2;
length_line3=sqrt((bx(1)-bx(2))^2+(by(1)-by(2))^2);
sina3=(by(1)-by(2))/length_line3;
cosa3=(bx(2)-bx(1))/length_line3;

VX_line1=interp2(VXm_geostr,xline1,yline1,'cubic');
VY_line1=interp2(VYm_geostr,xline1,yline1,'cubic');
%repeat for the other two vortices
VX_line2=interp2(VXm_geostr,xline2,yline2,'cubic');
VY_line2=interp2(VYm_geostr,xline2,yline2,'cubic');
VX_line3=interp2(VXm_geostr,xline3,yline3,'cubic');
VY_line3=interp2(VYm_geostr,xline3,yline3,'cubic');

Vazimuthal1=VX_line1*sina1+VY_line1*cosa1;
Vazimuthal2=VX_line2*sina2+VY_line2*cosa2;
Vazimuthal3=VX_line3*sina3+VY_line3*cosa3;

% Plot Vazimuthal versus Radius
figure(2)
plot(dd1,Vazimuthal1)
xlabel('Diameter(cm)');
ylabel('Azimuthal Velocity (cm/s)');
hold on

figure(3)
plot(dd2,Vazimuthal2)
xlabel('Diameter(cm)');
ylabel('Azimuthal Velocity (cm/s)');
hold on

figure(4)
plot(dd3,Vazimuthal3)
xlabel('Diameter(cm)');
ylabel('Azimuthal Velocity (cm/s)');
hold on

aaa=abs(Vazimuthal1);
bbb=abs(Vazimuthal2);
ccc=abs(Vazimuthal3);

aa=max(aaa)
bb=max(bbb)
cc=max(ccc)

save([geosVel_dir
vortexID],'aa','bb','cc','fname','VXm_geostr','VYm_geostr','Nx','Ny','Vazimut
hal1','Vazimuthal2','Vazimuthal3','dd1','dd2','dd3','diameter1','diameter2','
diameter3')
```

Filename: vortex_propspeed.m

```
%%%%%%%%%%%%%%%%%%%%%%%%%%%%%%%%%%%%%%%%%%%%%%%%%%%%%%%%%%%%%%%%%%%%%%%%%%%%%%%
% This file measures the distance and velocity of a vortex that is
% tracked from one frame to the following frame. It also generates images
% that indicate the initial position and the final position of the vortex.
% Sheilagh O'Leary, May 2010
% email: soleary@mun.ca
% fname = vortex_propspeed
%%%%%%%%%%%%%%%%%%%%%%%%%%%%%%%%%%%%%%%%%%%%%%%%%%%%%%%%%%%%%%%%%%%%%%%%%%%%%%%

% load previous results
cd (results_dir)
load ([endname_slide experID_calibr])
load(['tank_size_' experID_calibr])
load(['null_velocity_' experID_calibr])
cd (work_dir)

Nframe=1;

% scale in cm/pixel
scale=D/(px(2)-px(1));

%%%%%%%%%%%%%%%%%%%%%%%%%%%%%%%%%%%%%%%%%%%%%%%%%%%%%%%%%%%%%%%%%%%%%%%%%%%%%%%
% This section opens the video for analysis and allows the user to measure
% the wavelength of the baroclinic instabilities.
%%%%%%%%%%%%%%%%%%%%%%%%%%%%%%%%%%%%%%%%%%%%%%%%%%%%%%%%%%%%%%%%%%%%%%%%%%%%%%%

% load previous results
cd (results_dir)
load ([endname_slide experID_calibr])
load(['tank_size_' experID_calibr])
load(['null_velocity_' experID_calibr])
cd (work_dir)

Nframes=1;
count=0+nstart

% scale in cm/pixel
scale=D/(px(2)-px(1));

% first image with the vortex
hh=figure(1)
imshow(av.cdata)
title('Vortex image 1')
hold on

% prompts input points from the user from image 1
'Select the center of the vortex'
n = 1;
[pxx,pyy]=ginput(n);

% rename the input points so it's easier to handle them later. Add more
% points as n increases or decreases.
x1 = pxx(1);
```

```
y1 = pyy(1);
plot(x1,y1,'Color','r','Marker','+');

%%% open the second image, fname2
av=aviread(fullfile(dirname_movie,fname2),Nframe)

if(av_switch==1)
av2=aviread(fullfile(dirname_movie,fname2),Nframe:Nframe+Nav-1)
I=im2double(av2(1).cdata);
for j=1:Nav
    Iprev=I;
I= im2double(av2(j).cdata);
I=I+Iprev;
end
av.cdata=I/(Nav+1);
clear I Iprev av2
end
clear Ivideo_lab aimage bimage Ivideo_lab_2 aimage_2 bimage_2

av2=imcrop(av.cdata,[min([px(1) px(2)]) min([ py(3) py(4)]) sizx sizy]);
av2=imresize(av2, [sizxy sizxy],'bilinear');

C2 = makecform('srgb2lab');
Ivideo_lab= applycform(av2,C2);
Ivideo_lab = lab2double(Ivideo_lab);

% load previous results
cd (results_dir)
load ([endname_slide experID_calibr])
load(['tank_size_' experID_calibr])
load(['null_velocity_' experID_calibr])
cd (work_dir)

Nframes=1;
count=0+nstart

hh=figure(2)
imshow(av.cdata)
title('Vortex image 2')
hold on

'Select the center of the vortex'
n = 1;
[lxx,lyy]=ginput(n);
x2=lxx;
y2=lyy;

plot(x1,y1,'Color','r','Marker','+');
plot(x2,y2,'Color','b','Marker','+');

% distance calculation
% this is distance in cm because it is pixels*scale where scale is cm/pixel
disp=(sqrt(((x2-x1)^2)+((y2-y1)^2)))*scale

save([vortxxx_dir vorxID],'disp','fname','fname2','dirname_movie')
```

Filename: jet_measurement_soleary.m

```
%%%%%%%%%%%%%%%%%%%%%%%%%%%%%%%%%%%%%%%%%%%%%%%%%%%%%%%%%%%%%%%%%%%%%%%%%%%%%
% This file is supposed to measure the distance between selected points in
% a circular tank. A radius can also be selected and the points can be
% selected along this radius. The program then determines the azimuthal
% velocity at the points selected along the radius and plots the velocity
% versus radial distance.
% Sheilagh O'Leary, May 2009
% email: soleary@mun.ca
% fname = jet_measurement_soleary
%%%%%%%%%%%%%%%%%%%%%%%%%%%%%%%%%%%%%%%%%%%%%%%%%%%%%%%%%%%%%%%%%%%%%%%%%%%%%

% load previous results
cd (results_dir)
load ([endname_slide experID_calibr])
load(['tank_size_' experID_calibr])
load(['null_velocity_' experID_calibr])
cd (work_dir)

Nframe=1;

% scale in cm/pixel
scale=D/(px(2)-px(1));

%%%%%%%%%%%%%%%%%%%%%%%%%%%%%%%%%%%%%%%%%%%%%%%%%%%%%%%%%%%%%%%%%%%%%%%%%%%%%
% This section opens the video for analysis and allows the user to input
% the centre of the tank, input and measure the radius, and input the
% points where the jets lie along the radius and measure the distance
% between the jets.
%%%%%%%%%%%%%%%%%%%%%%%%%%%%%%%%%%%%%%%%%%%%%%%%%%%%%%%%%%%%%%%%%%%%%%%%%%%%%

% scale in cm/pixel
scale=D/(px(2)-px(1));

%%% velocity by color mapping
figure(1)
av2=imadjust(av2,stretchlim(av2),[]);
 imshow([1 Nx],[1 Ny], av2(1:Ny,1:Nx,:))
hold on

%plot geostrophic velocity
ymin2=1;
VYm_geostr(ymin2+nv:ymin2+nv+nv-1,1:nv)=0;
VXm_geostr(ymin2+nv:ymin2+nv+nv-1,1:nv)=velscale;

quiver(1 :nv:Nx, 1:nv:Ny,VXm_geostr(1:nv:Ny,1 :nv:Nx), VYm_geostr(1:nv:Ny,1
:nv:Nx,1))
title('Geostrophic velocity')

% mark the centre of the slide
'Mark the slide centre.'
nnx=Nx/2;
nny=Ny/2;
```

```
line(nnx,nny,'Marker','+');

% mark the radius
'Select the radius.'
[lx,ly]=ginput(2); %input the left and right points of the line
llx=lx;
lly=ly;
line(llx,lly)

c1=(ly(1)-ly(2))/(lx(1)-lx(2));
c2=(ly(2)*lx(1)-ly(1)*lx(2))/(lx(1)-lx(2));

stpp=abs(lx(2)-lx(1))/100;
xline=min(lx):stpp:max(lx);
yline=xline*c1+c2;
hold on
plot(xline,yline)

radius=(sqrt(((lx(2)-lx(1))^2)+((ly(2)-ly(1))^2)))*scale

st=(radius/100);
% create a vector for the radius of the tank
r = (0:st:radius);

% this section prompts the user to select the radius along which the
% distance between jets will be measured and the azimuthal velocity will be
% measured. Comment this section if you're just measuring distances between
% the baroclinic instabilities.'

% prompts input points from the user
'Select the jets'
n = 3;
[pxx,pyy]=ginput(n);
% the number of input points depends on the number of jets present in the
% video. right now, I assume n = 3 jets and that requires 3 input points.

% rename the input points so it's easier to handle them later
x1 = pxx(1);
y1 = pyy(1);
x2 = pxx(2);
y2 = pyy(2);
x3 = pxx(3);
y3 = pyy(3);

% distance calculation
% this is distance in cm because it is pixels*scale where scale is cm/pixel
distance1=(sqrt(((x2-x1)^2)+((y2-y1)^2)))*scale
distance2=(sqrt(((x3-x2)^2)+((y3-y2)^2)))*scale

% Find the azimuthal velocity at the points selected along the radius.
% this is for calculation of azimuthal velocity
length_line=sqrt((lx(1)-lx(2))^2+(ly(1)-ly(2))^2);
sina=(ly(1)-ly(2))/length_line;
cosa=(lx(2)-lx(1))/length_line;
```

```
VX_line=interp2(VXm_geostr,xline,yline,'cubic');
VY_line=interp2(VYm_geostr,xline,yline,'cubic');

Vazimuthal=VX_line*sina+VY_line*cosa;

% Plot Vazimuthal versus Radius
figure(2)
plot(r,Vazimuthal)
xlabel('Radius (cm)');
ylabel('Azimuthal Velocity (cm/s)');
hold on

save([jet_dir
experID],'VXm_geostr','VYm_geostr','Nx','Ny','VX_line','VY_line','Vazimuthal'
,'radius','distance1','distance2')
```

Filename: square_crop_soleary.m

```
%%%%%%%%%%%%%%%%%%%%%%%%%%%%%%%%%%%%%%%%%%%%%%%%%%%%%%%%%%%%%%%%%%%%%%%%%
% This file is supposed to measure rms velocity.
% Select a square region of the tank and then select 8 input points to
% calculate the RMS velocity.
% Sheilagh O'Leary, 2010
% email: soleary@mun.ca
% fname = square_crop_soleary
%%%%%%%%%%%%%%%%%%%%%%%%%%%%%%%%%%%%%%%%%%%%%%%%%%%%%%%%%%%%%%%%%%%%%%%%%

% load previous results
cd (results_dir)
load ([endname_slide experID_calibr])
load(['tank_size_' experID_calibr])
load(['null_velocity_' experID_calibr])
cd (work_dir)

Nframe=1;

% scale in cm/pixel
scale=D/(px(2)-px(1));

%%%%%%%%%%%%%%%%%%%%%%%%%%%%%%%%%%%%%%%%%%%%%%%%%%%%%%%%%%%%%%%%%%%%%%%%%
% This section opens the video for analysis.
% Section 1 was copied from main_calibration_29April
% Section 2 was taken from main_mapping to generate the geostrophic vorticity
% plot.

% This section allows the user to mark the centre of the tank, crop a square
% section of the image and then mark 8 points in the square section. The RMS
% velocity will be measured at each of the 8 selected points.

%%% velocity by color mapping
figure(1)
av2=imadjust(av2,stretchlim(av2),[]);
imshow([1 Nx],[1 Ny],av2(1:Ny,1:Nx,:))
hold on
%plot geostrophic velocity
ymin2=1;
VYm_geostr(ymin2+nv:ymin2+nv+nv-1,1:nv)=0;
VXm_geostr(ymin2+nv:ymin2+nv+nv-1,1:nv)=velscale;
quiver(1:nv:Nx,1:nv:Ny,VXm_geostr(1:nv:Ny,1
:nv:Nx),VYm_geostr(1:nv:Ny,1:nv:Nx,1))
title('Geostrophic velocity')

% mark the centre of the slide
'Mark the slide centre.'
nnx=Nx/2;
nny=Ny/2;
line(nnx,nny,'Marker','+');

'Select area to crop'
[pxc,pyc]=ginput(2); % input two corners of the rectangle to be cropped
```

```
line(pxc,pyc);
% show the sides of the selected rectangle
x1=pxc(1);
x2=pxc(2);
y1=pyc(1);
y2=pyc(2);
plot(x1,y1,'Color','r','Marker','+');
plot(x1,y2,'Color','y','Marker','+');
plot(x2,y1,'Color','b','Marker','+');
plot(x2,y2,'Color','g','Marker','+');

xwid=abs(pxc(1)-pxc(2))
yheight=abs(pyc(2)-pyc(1))

sizx_slide=xwid;
sizy_slide=yheight;
sizxy_slide=max([sizx_slide sizy_slide]);
% scales in cm/pixel
ascale=Lslide/sizxy_slide;
bscale=Lslide/sizxy_slide;

xmin=min([pxc(1) pxc(2)]);
ymin=min([pyc(1) pyc(2)]);

av=imcrop(av2,[x1 y1 xwid yheight]);
%av=imresize(av,[sizx_slide sizy_slide],'bilinear');
figure(2)
imshow(av)
% the cropped image is now displayed
'Select input points to calculate rms velocity'

npp=8; %the number of input points
[lx,ly]=ginput(npp); %input the points

lx1=lx(1);
ly1=ly(1);
lx2=lx(2);
ly2=ly(2);
lx3=lx(3);
ly3=ly(3);
lx4=lx(4);
ly4=ly(4);
lx5=lx(5);
ly5=ly(5);
lx6=lx(6);
ly6=ly(6);
lx7=lx(7);
ly7=ly(7);
lx8=lx(8);
ly8=ly(8);

VX_p1=interp2(VXm_geostr,lx1,ly1,'cubic');
VY_p1=interp2(VYm_geostr,lx1,ly1,'cubic');
VX_p2=interp2(VXm_geostr,lx2,ly2,'cubic');
VY_p2=interp2(VYm_geostr,lx2,ly2,'cubic');
```

```
VX_p3=interp2(VXm_geostr,lx3,ly3,'cubic');
VY_p3=interp2(VYm_geostr,lx3,ly3,'cubic');
VX_p4=interp2(VXm_geostr,lx4,ly4,'cubic');
VY_p4=interp2(VYm_geostr,lx4,ly4,'cubic');
VX_p5=interp2(VXm_geostr,lx5,ly5,'cubic');
VY_p5=interp2(VYm_geostr,lx5,ly5,'cubic');
VX_p6=interp2(VXm_geostr,lx5,ly5,'cubic');
VY_p6=interp2(VYm_geostr,lx5,ly5,'cubic');
VX_p7=interp2(VXm_geostr,lx5,ly5,'cubic');
VY_p7=interp2(VYm_geostr,lx5,ly5,'cubic');
VX_p8=interp2(VXm_geostr,lx5,ly5,'cubic');
VY_p8=interp2(VYm_geostr,lx5,ly5,'cubic');

u1=sqrt(((VX_p1^2)+(VY_p1^2))/2);
u2=sqrt(((VX_p2^2)+(VY_p2^2))/2);
u3=sqrt(((VX_p3^2)+(VY_p3^2))/2);
u4=sqrt(((VX_p4^2)+(VY_p4^2))/2);
u5=sqrt(((VX_p5^2)+(VY_p5^2))/2);
u6=sqrt(((VX_p5^2)+(VY_p5^2))/2);
u7=sqrt(((VX_p5^2)+(VY_p5^2))/2);
u8=sqrt(((VX_p5^2)+(VY_p5^2))/2);

urms=sqrt(((u1^2)+(u2^2)+(u3^2)+(u4^2)+(u5^2)+(u6^2)+(u7^2)+(u8^2))/npp)

line(lx1,ly1,'Color','r','Marker','+');
line(lx2,ly2,'Color','r','Marker','+');
line(lx3,ly3,'Color','r','Marker','+');
line(lx4,ly4,'Color','r','Marker','+');
line(lx5,ly5,'Color','r','Marker','+');
line(lx6,ly6,'Color','r','Marker','+');
line(lx7,ly7,'Color','r','Marker','+');
line(lx8,ly8,'Color','r','Marker','+');

save([geosVel_dir
squarecropID],'fname','VXm_geostr','VYm_geostr','Nx','Ny','u1','u2','u3','u4'
,'u5','u6','u7','u8','urms')
```

Filename: thickness_crop_feb2010.m

```
%%%%%%%%%%%%%%%%%%%%%%%%%%%%%%%%%%%%%%%%%%%%%%%%%%%%%%%%%%%%%%%%%%%%%%%%%%%%%
% script file:thickness_crop_feb2010.m
% Gives average layer thickness, H, for a selected rectangular area of the
% tank. Code by soleary@mun.ca, February 2010.
%%%%%%%%%%%%%%%%%%%%%%%%%%%%%%%%%%%%%%%%%%%%%%%%%%%%%%%%%%%%%%%%%%%%%%%%%%%%%
%  The first section (not shown) does color coding of surface elevations
% (slopes) taken from thickness.m.
%%%%%%%%%%%%%%%%%%%%%%%%%%%%%%%%%%%%%%%%%%%%%%%%%%%%%%%%%%%%%%%%%%%%%%%%%%%%%

%%% new figure!
figure(1);
imagesc(h11);
caxis([0 3]);
colorbar('location','southoutside')
title('My new image')

'Select area to crop'
[pxc,pyc]=ginput(2); % input two corners of the rectangle to be cropped
x1=pxc(1);
x2=pxc(2);
y1=pyc(1);
y2=pyc(2);
sizx_slide=abs(x2-x1);
sizy_slide=abs(y2-y1);
sizxy_slide=min([sizx_slide sizy_slide]);

H11=imcrop(h11,[min([x1 x2]) min([y1 y2]) sizx_slide sizy_slide]);
figure(2)
imagesc(H11);
caxis([0 3]);
colorbar('location','southoutside')
title('Layer thickness [cm]')

hh=H11;
hh(hh < 0) = []; %set negative numbers to 'empty'
hmean=mean(hh);
havg=mean(hmean)

save([thick_dir thickID],'hh','H11','havg','hmean')
```

Filename: instability_measurement.m

```
%%%%%%%%%%%%%%%%%%%%%%%%%%%%%%%%%%%%%%%%%%%%%%%%%%%%%%%%%%%%%%%%%%%%%%%%%%%%%%%
% This file is supposed to measure the distance between selected points in
% a circular tank. It was written to measure the wavelengths between
% baroclinic instabilities.
% Sheilagh O'Leary, May 2009
% email: soleary@mun.ca
% fname = instability_measurement
%%%%%%%%%%%%%%%%%%%%%%%%%%%%%%%%%%%%%%%%%%%%%%%%%%%%%%%%%%%%%%%%%%%%%%%%%%%%%%%

% load previous results
cd (results_dir)
load ([endname_slide experID_calibr])
load(['tank_size_' experID_calibr])
load(['null_velocity_' experID_calibr])
cd (work_dir)

Nframe=1;

% scale in cm/pixel
scale=D/(px(2)-px(1));

%%%%%%%%%%%%%%%%%%%%%%%%%%%%%%%%%%%%%%%%%%%%%%%%%%%%%%%%%%%%%%%%%%%%%%%%%%%%%%%
% This section opens the video for analysis and allows the user to measure
% the wavelength of the baroclinic instabilities.

% This section was copied from main_calibration_29April.m. It opens the image
% from the selected video for analysis.

% load previous results
cd (results_dir)
load ([endname_slide experID_calibr])
load(['tank_size_' experID_calibr])
load(['null_velocity_' experID_calibr])
cd (work_dir)

Nframes=1; %info.NumFrames;
count=0+nstart

% scale in cm/pixel
scale=D/(px(2)-px(1));

hh=figure(1)
imshow(av.cdata)

% prompts input points from the user. Change "n" depending on the number of
% instabilities you need to measure.
'Select the baroclinic instabilities'
n = 3;
[pxx,pyy]=ginput(n);

% rename the input points so its easier to handle them later. Add more
% points as n increases or decreases.
```

```
x1 = pxx(1);
y1 = pyy(1);
x2 = pxx(2);
y2 = pyy(2);
x3 = pxx(3);
y3 = pyy(3);
%x4 = pxx(4);
%y4 = pyy(4);
%x5 = pxx(5);
%y5 = pyy(5);

% distance calculation
% this is distance in cm because it is pixels*scale where scale is cm/pixel
% Add more distance measurements as n increases.
baro1=(sqrt(((x2-x1)^2)+((y2-y1)^2)))*scale
baro2=(sqrt(((x3-x2)^2)+((y3-y2)^2)))*scale
%baro3=(sqrt(((x4-x3)^2)+((y4-y3)^2)))*scale
%baro4=(sqrt(((x5-x4)^2)+((y5-y4)^2)))*scale

%change this to include all distances that were measured.
save([inst_dir experID],'baro1','baro2')%,'baro3')%,'baro4')
```